FISEVIER

Contents lists available at ScienceDirect

Journal of Wind Engineering & Industrial Aerodynamics

journal homepage: www.elsevier.com/locate/jweia



Automated terrain generation for precise atmospheric boundary layer simulation in the wind tunnel



R.A. Catarelli ^a, P.L. Fernández-Cabán ^b, F.J. Masters ^{a,*}, J.A. Bridge ^a, K.R. Gurley ^a, C.J. Matyas ^c

- ^a Department of Civil and Coastal Engineering, University of Florida, Gainesville, FL, 32611, USA
- ^b Department of Civil and Environmental Engineering, Clarkson University, Potsdam, NY, 13699, USA
- ^c Department of Geography, University of Florida, Gainesville, FL, 32611, USA

ARTICLE INFO

Keywords:
Boundary layer
Wind tunnel
Commissioning
Morphometric
Roughness length
Displacement height

ABSTRACT

This study presents a two-stage framework to characterize boundary layer wind tunnel (BLWT) approach flows naturally developed over grid roughness for partial atmospheric boundary layer (ABL) simulation. The first stage applies curve fitting techniques to a comprehensive series of high-resolution spatially-averaged velocity profile measurements to estimate aerodynamic roughness parameters (ARPs) for a wide range of homogeneous (i.e., equal height) roughness element configurations. For this study, an automated (i.e., computer-controlled) 62×18 roughness element array called the Terraformer was used to generate 33 unique roughness element fields. The mean flow structure was captured downwind to the Terraformer, where key ARPs-i.e., the urban canopy attenuation coefficient, zero-plane displacement height, shear (friction) velocity, roughness length, and Coles' wake strength coefficient—were estimated. In contrast to previous ABL modeling methods that primarily focused on curve fitting of the inertial sublayer (ISL), the proposed approach applies the urban canopy exponential profile within the roughness sublayer (RSL), the log law in the ISL, and the law of the wake in the outer wake layer to model full-depth (i.e., floor to freestream) rough-wall turbulent boundary layers. Further, the method explicitly captures potential variability of Reynolds shear stress in the ISL and the wake strength in the outer layer to generalize characterization of naturally-developed BLs produced by traditional tunnel designs. The second stage applies a morphometric model for each ARP—calibrated with estimates from Stage 1—to predict flow characteristics for a wide range of roughness element configurations, with the goal of producing a deterministic solution for selecting an element configuration to satisfy user-specified aerodynamic objectives for the approach flow. The calibrated models effectively interpolate between estimates, e.g., ARPs estimated for open and suburban terrains can be applied in the second stage model calibration to predict ARPs for a "rough-open" condition without further experimentation. The findings of this study demonstrate that coupling the proposed framework with a mechanized roughness element grid can significantly reduce the trial-and-error required to commission a BLWT, while improving the quality of flow characterization.

1. Introduction

This paper presents a framework to characterize "floor to freestream" upwind approach flows naturally developed over a roughness element array of uniform height in a boundary layer wind tunnel (BLWT) for partial atmospheric boundary layer (ABL) simulation. The conventional method for achieving user-specified aerodynamic objectives is to iteratively adjust the geometric dimensions and/or spacing of the roughness elements until similarity requirements—e.g., the longitudinal profiles of mean velocity and turbulence intensity—are met (Counihan, 1969; Cook,

1978; Gartshore and De Croos, 1977). Although straightforward, this time-intensive process yields only one calibrated approach flow and is generally not extensible to other wind tunnel facilities. Variations in experimental configurations may, in part, explain why recent BLWT measurement comparisons (e.g., Cheng et al., 2007; Karimpour et al., 2012; Mohammad et al., 2015) differ in results.

The proposed framework serves as a two-stage rational design aide to define the mean flow structure in the inner wall and outer wake layers. The first stage estimates the following aerodynamic roughness parameters (ARPs):

E-mail addresses: rcatarelli@ufl.edu (R.A. Catarelli), pfernand@clarkson.edu (P.L. Fernández-Cabán), masters@ce.ufl.edu (F.J. Masters), jennifer.bridge@essie.ufl.edu (J.A. Bridge), kgurl@ce.ufl.edu (K.R. Gurley), matyas@ufl.edu (C.J. Matyas).

^{*} Corresponding author.

Nomenc	lature	147	roughness element vertical facets
/\	lataral anatial assurating an ameter	W_{y}	across-wind horizontal distance between adjacent
$\langle \rangle$	lateral spatial averaging operator	77	roughness element vertical facets
4	prediction operator	X	fetch length
A_d	roughness element lot area	x, y, z	longitudinal, lateral, and vertical spatial coordinates within
A_f	roughness element frontal area		the wind tunnel, respectively
A_p	roughness element plan area	z_I	two-state model interface position
a	attenuation coefficient	z_w	wake diffusion height
C_D	obstacle drag coefficient	z_0	roughness length
c_1, c_2, c_3	outer layer curve fitting constants	Greek Sy	mhols
D_x	along-wind horizontal spacing between roughness elements	α	drag correction factor
D_{y}	across-wind horizontal spacing between roughness	β	sheltering effect factor
	elements	δ	gradient height
d	zero-plane displacement height	δ_0	gradient height initial guess
F_D	from drag	Ü	mean of interface position
h	roughness element height	μ_{z_I}	standard deviation of interface position
I_u, I_v, I_w	longitudinal, lateral, and vertical turbulence intensity	σ_{z_I}	
L_x	along-wind horizontal dimension of roughness element	$\sigma_u, \sigma_v, \sigma_w$	deviation
L_{y}	across-wind horizontal dimension of roughness element	κ	von Kármán's constant (0.4)
Re_*	surface-roughness Reynolds number	$\lambda_{\rm f}$	frontal area index
U, V, W	mean velocity components in x , y , and z directions,	$\lambda_{\rm p}$	plan area index
	respectively		kinematic viscosity of air
U_h	longitudinal mean velocity at element height	ν Π	Cole's wake strength coefficient
U_δ	longitudinal mean velocity at gradient height		mass density of air
u, v, w	instantaneous velocity components in x , y , and z directions,	ρ	mean wall shear stress
	respectively	$ au_0$	Reynolds shear stress
u', v', w'	mean-removed fluctuating velocity components	$ au_{R_{xz}}$ $oldsymbol{\Phi}$	Gaussian cumulative distribution function
u*	shear (friction) velocity	_	wake function
W_x	along-wind horizontal distance between adjacent	ω	wake function

- attenuation coefficient in the urban canopy (a)
- zero-plane displacement height (d)
- shear (friction) velocity (u_*)
- roughness length (z₀)
- Coles' wake strength coefficient in the outer wake layer (Π)

from fast-response 3D anemometric data for a discrete set of roughness element configurations. The second stage applies morphometric modeling and calibration techniques to Stage 1 results, obtained from multiple terrains, to predict the mean flow structure for the entire range of roughness element heights without the need of additional flow measurements.

In this study, model predictions were calibrated with anemometric data collected downwind of an automated 1116 roughness element array called the Terraformer, which can vertically translate elements 0–160 mm and rotate them 360°. Velocity profiles were obtained for 33 unique homogeneous terrain conditions at the downwind terminus of the development section (i.e., a measurement station in the tunnel immediately upwind of the test section). After calibration of morphometric models, strong agreement was observed between ARP estimates and predictions across all terrain cases. Further, we also successfully demonstrate how this approach can be extended to model the longitudinal turbulence intensity profile for all element heights. The ultimate product is a deterministic "lookup" for a BLWT operator to select an element height and orientation for a specified geometric scale and set of ARP requirements.

The paper demonstrates that combining the proposed framework with an automated roughness element array can significantly decrease or even eliminate time-intensive trial-and-error required to achieve user-specified flow similarity requirements, opening a pathway to conduct high-throughput experimentation across a wide range of turbulence regimes. The approach is recommended for adoption in BLWT commissioning standards such as ASCE/SEI 49-12 and AWES-QAM-1-2019.

2. Partial ABL simulations in wind tunnels

Accurate estimation of ARPs (particularly z_0 and d) is essential for meteorological and wind engineering applications, e.g., dispersion of pollutants, environmental wind effects, wind-induced structural loads on civil infrastructure, and siting of wind energy resources. Errors can lead to large variations in surface pressures and other critical measurements. Thus BLWT operators must carefully "tune" these parameters by adjusting the density of roughness elements in the development section to achieve the desired aerodynamic objectives at the test section.

The primary ABL similitude target of the current study is the neutrally-stratified longitudinal mean velocity (U) profile, where the vertical gradient of U is positive ($\partial U/\partial z>0$) and the vertical flux of longitudinal momentum is negative ($\overline{u'w'}<0$)—a condition that is valid for wall-bounded turbulent shear flows. The ABL is typically grown over significant fetch lengths of many kilometers at full-scale. However, BLWT development sections are almost without exception too short in length—potentially by a factor of 2–5 based on empirical models (e.g., Panofsky and Dutton, 1983)—to produce naturally-developed geometrically scaled full-depth ABL flow simulations (De Bortoli et al., 2002), and measurements of the U profile from "floor to freestream" reveal the inner wall layer (i.e., the useable region for tests) and the (unusable) outer wake layer, where the flow transitions from a rough-wall boundary layer to a freestream condition (Fig. 1).

The inner wall layer consists of the viscous, roughness, and inertial sublayers, with the roughness sublayer (RSL) extending vertically from the top of the viscous sublayer to the wake diffusion height z_w (Coceal et al., 2007). In a region within the RSL called the urban canopy layer (UCL), the U profile from $0 < z \le h$ approximately follows the exponential form given by Cionco (1965):

$$U(z) = U_h \exp[a(z/h-1)]$$
 (1)

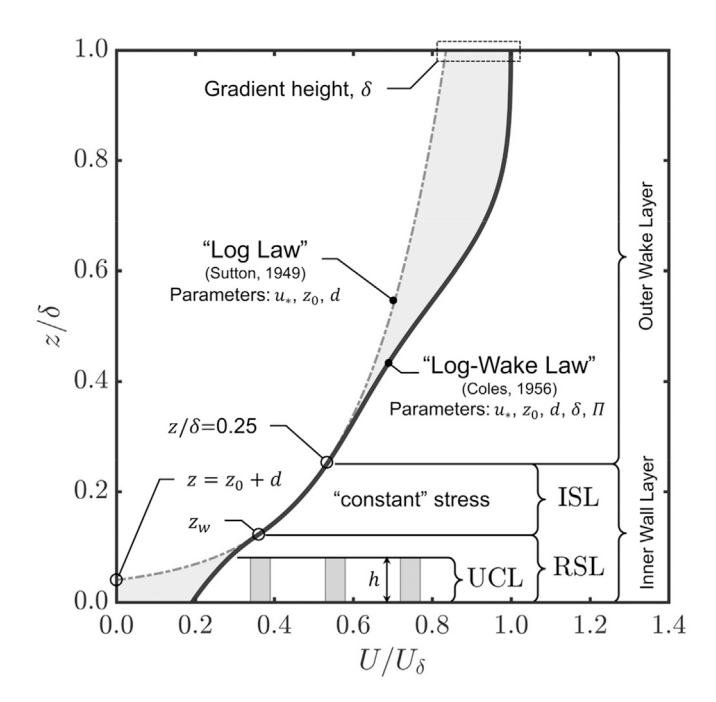


Fig. 1. Typical rough-wall wind tunnel BL U profile. Viscous sublayer not shown.

where U_h is the mean velocity at the roughness element height h. Local sheltering effects of the roughness element wakes are present in the UCL (Raupach et al., 1980; Macdonald, 2000; Bentham and Britter, 2003), thus Eq. (1) represents a lateral average of multiple adjacent U profiles collected at a selected longitudinal measurement station (e.g., Macdonald et al., 1998b).

At the upper limit of the RSL, which generally ranges from $1.3 < z_w/h < 2.5$ (Macdonald, 2000), turbulent mixing sufficiently blends the individual element wakes to produce laterally homogeneous flow. The height that this occurs (z_w) represents the lower limit of the inertial sublayer (ISL), i.e. the constant Reynolds shear stress $(\tau_{R_{xz}} = -\rho \overline{u'w'})$ region of a neutral BL. In the BLWT, however, $\tau_{R_{xz}}$ may vary with height except for precisely controlled longitudinal zero-pressure-gradient (ZPG) flows—a variation accounted for in the proposed framework.

The ISL nominally exists between $z_w < z < 0.25\delta$, where δ is the BL depth or gradient height (Raupach et al., 1980; Macdonald, 2000; Cheng et al., 2007). The U profile in this sublayer is described by the log law modified by Sutton (1949) to include d (i.e., the effective floor elevation):

$$U(z) = \frac{u^*}{\kappa} \ln \left(\frac{z - d}{z_0} \right) \tag{2}$$

where $\kappa=0.4$ is von Kármán's constant. This equation holds under the following conditions: the surface is aerodynamically fully-rough—i.e., the surface-roughness Reynolds number $Re^*=u^*z_0/\nu\geq 2.5$ (Sutton, 1953; Schlichting, 1979), where ν is the kinematic viscosity of air; the blockage ratio $\delta/h\geq 5$ (Castro, 2007); and the freestream turbulence (FST) level is below 4% (Hancock and Bradshaw, 1983; Thole and Bogard, 1996). From Weber (1999), the shear velocity is given as:

$$u_* = \sqrt{\tau_0/\rho} = \left(\overrightarrow{u}\overrightarrow{w}^2 + \overrightarrow{v}\overrightarrow{w}^2\right)^{1/4}\Big|_{z_w < z < 0.25\delta}$$
(3)

where τ_0 is the mean wall shear stress, ρ is the mass density of air, and u', v', w' are mean-removed fluctuating velocity components at a measurement height z within the ISL (Manes et al., 2011). Given that the horizontal Reynolds stress vector aligns with the principle flow direction in the (ducted) wind tunnel, Eq. (3) reduces to

$$u^{z} = \sqrt{|\overrightarrow{u'w'}|}\Big|_{z_{w} < z < 0.25\delta} \tag{4}$$

Equations (3) and (4) hold provided that $\tau_{R_{xx}}$ is constant with height in the ISL. Above $z \cong 0.25\delta$ (the outer wake layer), the longitudinal velocity profile deviates from Eq. (2), exhibiting higher mean velocities and lower turbulence intensities than those predicted by the log law alone (Coles, 1956). Flow properties are governed by both the law of the wall (i.e., the log law) and the law of the wake—in the form of the log-wake law:

$$U(z) = \frac{u_*}{\kappa} \left[\ln \left(\frac{z - d}{z_0} \right) + \Pi \omega \left(\frac{z - d}{\delta - d} \right) \right]$$
 (5)

where ω is the generic wake function normalized such that $\omega(1)=2$ for ZPG flows (Jiménez, 2004; Castro, 2007; Yang et al., 2016). At $z=\delta$, the U profile deviation from the log law is $2\Pi u^{s}/\kappa$. Above the outer wake layer $(z>\delta)$ is the freestream condition, where the influence of shear stress from the roughness grid becomes negligible (i.e., $\tau_{R_{xx}}\cong 0$) and the U profile is approximately constant with height.

2.1. Methods for estimating surface roughness of obstacle arrays

Estimates of z_0 and d for a given roughness array are typically obtained through morphometric or anemometric approaches, e.g., Grimmond and Oke (1999); Karimpour et al. (2012). Morphometric methods estimate the values based on roughness element shape and arrangement using empirical relationships derived from wind tunnel experiments (Lettau, 1969; Bottema, 1997; Macdonald et al., 1998a). Anemometric methods (e.g., Barlow et al., 1999) and curve fitting techniques are used to match the log law to velocity profile measurements in the wind tunnel.

2.1.1. Fitting of anemometric data

Many well-established methods exist for quantifying ARPs from U profile measurements, e.g., Farell and Iyengar (1999); Coceal et al. (2006); Kanda and Moriizumi (2009). ARPs are obtained by fitting Eq. (2) to the measured U profile in the "constant" stress region. Mohammad et al. (2015) classifies these methods into three general categories, with the one and two parameter models being incorporated here:

- In the three parameter (3P) method, a non-linear fit is applied to measured profile data, where u^* , z_0 , and d are treated as free fitting parameters. This method can accurately estimate u^* in smooth BL flows where d is negligible and z_0 is relatively small (Theurer et al., 1992). However, in rougher upwind conditions, 3P fitting will yield unrealistic roughness values (e.g., negative d) due to the ill-conditioned nature of Eq. (2) and the strong correlations between the three parameters (Legg et al., 1981). As a result, d is typically bounded when fitting the data (Cheng et al., 2007)
- The two-parameter (2P) fitting method reduces the uncertainty associated with the ill-fitting condition by independently estimating u* through surface pressure drag (Cheng et al., 2007) or Reynolds stress measurements, leaving only z_0 and d as fitting parameters
- The one-parameter (1P) method fits z_0 from the log law, where both u_* and d are obtained through experimental techniques—e.g., Reynolds stress measurements and center-of-pressure methods (Raupach et al., 1986)

2.1.2. Morphometric models

Morphometric models (e.g., Kutzbach, 1961; Wooding et al., 1973; Raupach, 1992; Bottema, 1995; Grimmond and Oke, 1999; Shao and Yang, 2008; Yang et al., 2016) apply empirical relationships derived from wind tunnel simulations of idealized rough surfaces to predict z_0 and d from geometric parameters. The approach is suitable for characterizing flows over regular geometries such as the generic obstacle array shown in Fig. 2.

Regular obstacle arrays produce three distinct flow regimes delin-

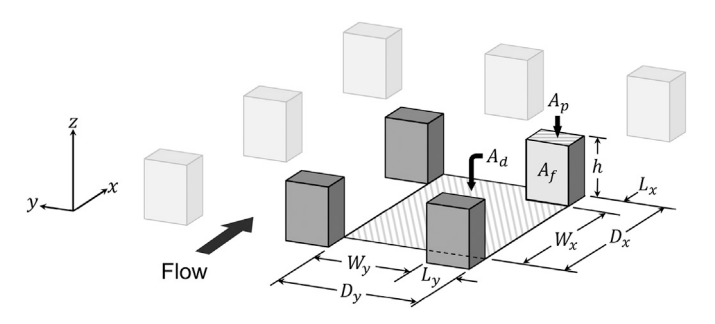


Fig. 2. Surface geometric parameters used in morphometric analysis of regular obstacle arrays.

eated by area density λ (Hussain and Lee, 1980; Oke et al., 2017): isolated flow ($W_x/h > 3.33$), where elements are spaced sufficiently far apart to produce fully-developed wakes and separation bubbles; wake interference flow (1.53 $< W_x/h < 3.33$), where element wakes are reinforced through mutual interactions; and skimming flow ($W_x/h < 1.53$), where elements are spaced closely and flow no longer strongly interacts with the element grid. Wake interference flow is likely to produce the greatest roughness effects and, as is the case here, typically selected for wind tunnel simulations of the ABL (Grimmond and Oke, 1999).

Most morphometric models incorporate secondary geometric parameters (Plate, 1995) to couple roughness grid geometries to z_0 and d. In this study, we apply the frontal area density λ_f and plan area density λ_p :

$$\lambda_{\rm f} = \frac{A_{\rm f}}{A_{\rm d}} \tag{6}$$

$$\lambda_{p} = \frac{A_{p}}{A_{s}} \tag{7}$$

where the element frontal area $A_f = hL_y$, the element plan area $A_p = L_xL_y$, and the roughness element lot area $A_d = D_xD_y$ as shown in Fig. 2.

3. Methodology

Table 1 presents the procedure to estimate ARPs from velocity profile data (Section 3.1) and calibrate morphometric model predictions based on Macdonald et al. (1998a) and Yang et al. (2016).

3.1. ARP estimation from velocity profile data (Stage I)

ARP estimates are obtained from velocity profiles measured over a discrete set of roughness element configurations of incrementally increasing density. This process reveals the pattern of BL profile modulation induced by changes in roughness. In the context of this paper, an estimate refers to a parameter value resulting from a profile fit or other process of directly analyzing velocity data.

 $\begin{tabular}{ll} \textbf{Table 1}\\ Framework to estimate aerodynamic parameters and calibrate model predictions. \end{tabular}$

Section (Stage)	Subsection	Parameter(s)	Procedure
3.1. ARP estimation from velocity profile data (Stage I)	1	δ , U_{δ}	Polynomial fit near BL margin
	2	а	Least-squares fit to UCL
	3	d	Center-of-pressure theorem (COP)
	4	u*	Reynolds shear stress profile extrapolation (RSSPE)
	5	z_0	1P least-squares fit to log law
	6	П	Two-state model least-squares fit to outer layer
3.2. Morphometric model calibration from ARP estimates (Stage II)	1	\widehat{a}	Attenuation coefficient model fit to estimated a
	2	\widehat{d}/h	Analytical center-of-pressure (COP) evaluation
	3	\widehat{z}_0/h	Macdonald et al. (1998a) z ₀ morphometric model
	4	\widehat{u}_*/U_h	Log law rearrangement given \hat{d}/h and \hat{z}_0/h

3.1.1. Gradient height (δ) and gradient velocity (U_{δ})

The first step estimates the gradient height, gradient velocity, and ISL depth. The outer layer of the U profile, which is approximately parabolic in shape near the BL margin, is fitted by the quadratic function defined in Guo (1998). The initial guess for the gradient height δ_0 (i.e., where $\partial U/\partial z=0$) is selected from visual inspection of data. The mean velocity is then fit to the range $0.5\delta_0 < z < \delta_0$ following:

$$U(z) = c_1 z^2 + c_2 z + c_3 (8)$$

where c_1 , c_2 , c_3 are coefficients determined by minimizing the root-mean-square error (RMSE):

$$RMSE_{c_1,c_2,c_3} = \sqrt{\frac{1}{N} \sum_{i=1}^{N} \left[\langle U \rangle_i - (c_1 z_i^2 + c_2 z_i + c_3) \right]^2}$$
 (9)

where $\mathrm{RMSE}_{c_1,c_2,c_3}$ is the minimum value produced by the best estimates of c_1 , c_2 , and c_3 . The value U_i is the measured mean velocity at height z_i in the specified region and the angle brackets " $\langle \rangle$ " indicate laterally (i.e., y-direction) averaged values. The value δ is found by setting $\partial U/\partial z=0$:

$$\delta = -\frac{c_2}{2c_1} \tag{10}$$

The gradient velocity U_{δ} is estimated by evaluating Eq. (8) at $z = \delta$ using the result from Eq. (10):

$$U_{\delta} = c_1 \delta^2 + c_2 \delta + c_3 \tag{11}$$

Following Raupach et al. (1980), Macdonald (2000), and Cheng et al. (2007), the location of the ISL upper limit is estimated as $z = 0.25\delta$.

3.1.2. Attenuation coefficient (a)

Flow in the UCL, which is strongly influenced by the roughness grid geometry, is characterized by fitting Eq. (1) to $\langle U \rangle$ profile data from $0 < z \le h$. The curvature of the spatially-averaged profile is defined by the shape parameter a—estimated by minimizing the RMSE:

$$RMSE_{a} = \sqrt{\frac{1}{N} \sum_{i=1}^{N} \left[\langle U \rangle_{i} - \langle U_{h} \rangle exp[a(z_{i}/h - 1)] \right]^{2}}$$
 (12)

where RMSE_a is the value produced by the best estimate of a. To fit this expression, $\langle U_h \rangle$ must be directly measured at z=h, and $\lambda_f < 0.3$ —i.e., prior to the onset of skimming flow, where Eq. (1) is no longer a good fit to $\langle U \rangle$ data (Macdonald, 2000).

3.1.3. Zero-plane displacement height (d)

No consensus currently exists for a physical definition of *d*, despite its extensive study (e.g., Iyengar and Farell, 2001; Raupach et al., 2006; Coceal et al., 2007; Jiang et al., 2008). However, the center-of-pressure

(COP) theorem first formalized by Thom (1971)—which equates d with the mean level of momentum absorption or, equivalently, the height at which the mean drag appears to act on the roughness element grid—was rigorously demonstrated by Jackson (1981). Following Raupach et al. (1986), Leonardi and Castro (2010), and Böhm et al. (2013), the COP definition is applied in this framework to decouple the calculations of z_0 and d as follows:

$$d = \left(\int_0^h z F_D(z) dz \right) / \left(\int_0^h F_D(z) dz \right)$$
 (13)

With the assumption that form drag F_D is the main mechanism of momentum transfer within the UCL for regular roughness element arrays (Thom, 1971; Raupach et al., 1986; Böhm et al., 2013), the distributed drag force relation is written as:

$$F_D(z) = \partial/\partial z [\langle \overline{u} \, \overline{w} + \overline{u}, \overline{w}, \rangle] = -\frac{1}{2} C_D(z) A(z) U(z)^2$$
(14)

where $\langle \overrightarrow{uw} + \overrightarrow{u}''\overrightarrow{w}'' \rangle$ is the total momentum flux, $\overrightarrow{u}''\overrightarrow{w}''$ is the dispersive flux, $C_D(z) = \langle \Delta P \rangle(z)/\frac{1}{2}\rho \langle U \rangle(z)^2$ is the sectional drag coefficient as a function of height $(0 < z \le h)$, $\langle \Delta P \rangle(z)$ is the longitudinal mean static pressure difference laterally averaged across each roughness element, and $A(z) = \lambda_f/h$ is the element frontal area per unit volume, which is constant for regular cuboid roughness element arrays. Substituting the first F_D definition of Eq. (14) into Eq. (13), the COP theorem is given as:

$$d = \left(\int_0^h z (d\langle \overline{u'w'} + \overline{u}', \overline{w}', \rangle/dz) dz \right) / \left(\int_0^h (d\langle \overline{u'w'} + \overline{u}', \overline{w}', \rangle/dz) dz \right)$$
(15)

Assuming that $\langle \overline{u'w'} + \overline{u''}\overline{w''} \rangle|_{z=0} \ll \langle \overline{u'w'} + \overline{u''}\overline{w''} \rangle|_{z=\hbar} = u_*^2$ for canopy flows (Brunet et al., 1994; Coceal et al., 2007) and C_D is constant, Eq. (15) reduces to

$$d = h - \left[\frac{1}{u^{2}}\right] \int_{0}^{h} \langle \overrightarrow{u'w'} + \overrightarrow{u}''\overrightarrow{w}'' \rangle dz$$
 (16)

where $u^{*2} = \frac{\lambda_f}{2\hbar} C_D \int_0^h \langle U \rangle (z)^2 dz$. The term $\langle \overline{u}'' \overline{w}'' \rangle$ is difficult to accurately determine experimentally, thus an alternative measurement is preferable. An approach that is less difficult to implement using common velocity profile measurement methods is to apply the second F_D definition of Eq. (14) to Eq. (13):

$$d = \left(\int_0^h z C_D(z) \langle U \rangle(z)^2 dz \right) / \left(\int_0^h C_D(z) \langle U \rangle(z)^2 dz \right)$$
 (17)

which provides a comprehensive estimate of d. However, determining $C_D(z)$ requires simultaneous pressure measurements of $\langle \Delta P \rangle(z)$ from $0 < z \le h$ or prior knowledge of the drag profile behavior for a given roughness configuration. In the absence of direct pressure measurements, the vertical variation in drag is difficult to predict (Lien and Yee, 2005; Leonardi and Castro, 2010) as it can take on a monotonic, unimodal, or bimodal shape (Brunet et al., 1994; Castro, 2017; Ramirez et al., 2018). For very low area densities (λ), the assumption that $C_D(z)$ exhibits little variation with height works well (see Castro, 2017). Nevertheless, as λ increases, non-negligible dispersive fluxes and high levels of drag near the wall may act to reduce d (Cheng et al., 2007) prior to the onset of skimming flow. Thus, the framework indirectly accounts for the potential vertical variation in drag within the canopy by applying an empirical correction, which reduces Eq. (17) to

$$d = \alpha \left(\int_0^h z \langle U \rangle(z)^2 dz \right) / \left(\int_0^h \langle U \rangle(z)^2 dz \right)$$
 (18)

where α is a drag correction factor adapted from Shaw and Pereira (1982), which in this case is the ratio of Eq. (17) evaluated with a varying $C_D(z)$ over the same equation with C_D set as a constant. The value of this correction factor was found to range from approximately $0.4 \le \alpha \le 1$ based on analysis of $C_D(z)$ models from Mache (2012) and Tian (2018) with comparisons to Lien and Yee (2005), Leonardi and Castro (2010), and Castro (2017) for both sparse and dense arrays of roughness elements. With α correcting for the vertical variation in drag, numerical integration of $\langle U \rangle$ profile data within the UCL is then used to determine d.

3.1.4. Shear velocity (u*)

In fully-developed ZPG BL flows, $\overrightarrow{u'w'}$ is not expected to vary with height in the ISL-a conclusion resulting from the temporally and spatially-averaged momentum equation for 2D ideal steady flow over a rough wall (Finnigan, 2000; Coceal and Belcher, 2004; Cheng et al., 2007), which yields $-\rho \partial \langle \overrightarrow{u'w'} \rangle / \partial z = 0$ and thus $\overrightarrow{u'w'} = \text{constant}$. However, Cheng et al. (2007) observed vertical variations in $\overline{u'w'}$ during wind tunnel experiments comprising a range of surface roughness densities and a fixed-pitch ceiling. These observations were attributed to non-zero longitudinal pressure gradients where the wind tunnel freestream cross-section decreases due to the natural growth of the BL, causing an increase in the freestream velocity and a loss in static pressure along the length of the development section. If these conditions exist in a BLWT experiment, the resulting momentum equation will be $-\rho\partial\langle \overrightarrow{u'w'}\rangle/\partial z =$ $\rho(U\partial U/\partial x + W\partial U/\partial z) + \partial P/\partial x + \rho\partial \langle \overline{u^{2}} \rangle/\partial x$, where $\partial U/\partial x$, $\partial U/\partial z$, $\partial P/\partial x$, and $\partial \langle \overline{u^{2}} \rangle/\partial x$ are the gradients of U, vertical mean velocity W, longitudinal mean static pressure P, and longitudinal Reynolds normal stress $\overline{u^{2}}$, respectively.

To accommodate for the vertical variation of $\overline{u\,w}$ observed in many wind tunnel studies (e.g., Raupach et al., 1986; Farell and Iyengar, 1999; Castro et al., 2006; Böhm et al., 2013; Placidi and Ganapathisubramani, 2015), we apply the linear varying Reynolds shear stress profile extrapolation (RSSPE) given in Cheng et al. (2007). This can be expressed as RSSPE(z) = $\overline{u\,w}(z) = (z-b_{\text{RSSPE}})/m_{\text{RSSPE}}$, where m_{RSSPE} is the slope and b_{RSSPE} is the z-intercept of the linear fit in the ISL region (lower and upper bounds defined in Section 2) to profile data obtained from fast response anemometric measurements of u', v', w'. The resulting fitted profile is then extrapolated down to the zero-plane level (z=d) to obtain shear velocity:

$$u_* = \sqrt{|RSSPE|}\Big|_{z=d} \tag{19}$$

This is a generalizable approach—consistent with direct drag force measurements (Cheng et al., 2007)—for variable as well as approximately constant \overrightarrow{uw} profiles. For the case of a classical fully-developed rough-wall BL, where \overrightarrow{uw} is height-invariant (i.e., constant), the result of Eq. (19) will be approximately equivalent to a vertical average of \overrightarrow{uw} in the ISL. The vertical $\tau_{R_{xx}}$ gradient need not be known a priori to apply the method.

3.1.5. Roughness length (z_0)

After d and u^* are obtained, z_0 is estimated using a 1P fitting of N spatially-averaged $\langle U \rangle$ profile data points located within the ISL. For curve fitting purposes, the lower limit has been shown to extend downward into the RSL to a height z=h provided the data are spatially-averaged (Cheng et al., 2007; Yang et al., 2016). The RMSE is determined from $\langle U \rangle$ and Eq. (2) using the following expression:

$$RMSE_{z_0} = \sqrt{\frac{1}{N} \sum_{i=1}^{N} \left[\langle U \rangle_i - \frac{u_*}{\kappa} \ln \left(\frac{z_i - d}{z_0} \right) \right]^2}$$
 (20)

where RMSE_{z_0} is the minimum value produced by the best estimate of z_0 .

3.1.6. Wake strength coefficient (Π)

Conventional methods to fit the U profile shape in the outer wake layer use a range of empirically derived wake functions (ω) described in Rona and Grottadaurea (2010). In contrast, the proposed framework applies a physically motivated two-state convolution of mean BL flow assuming it is a random independent process following Krug et al. (2017). The first state is the inertial region—pure wall flow—and the second is the free stream state joined at an interface position z_I . It is defined as:

$$U(z) = \frac{u_s}{\kappa} \ln\left(\frac{z - d}{z_0}\right) (1 - \mathbf{\Phi}) + U_\delta \mathbf{\Phi}$$
 (21)

where Φ is the Gaussian cumulative distribution function:

$$\Phi\left(\frac{z-\mu_{z_l}}{\sigma_{z_l}}\right) = \frac{1}{2} \left[1 + \operatorname{erf}\left(\frac{z-\mu_{z_l}}{\sigma_{z_l}\sqrt{2}}\right) \right]$$
 (22)

and μ_{z_l} and σ_{z_l} are the mean and standard deviation of z_l , respectively. These secondary parameters are determined by minimizing the RMSE of a curve fit to $\langle U \rangle$ profile data from $h \leq z \leq \delta$:

$$RMSE_{\mu_{z_I},\sigma_{z_I}} = \sqrt{\frac{1}{N} \sum_{i=1}^{N} \left[\langle U \rangle_i - \left(\frac{u_*}{\kappa} \ln \left(\frac{z_i - d}{z_0} \right) (1 - \boldsymbol{\Phi}) + U_{\delta} \boldsymbol{\Phi} \right) \right]^2}$$
 (23)

where $\text{RMSE}_{\mu_{z_l}, \sigma_{z_l}}$ is the value produced by the best estimates of μ_{z_l} and σ_{z_l} . Π is then be determined by:

$$\Pi = \frac{\Phi_{\delta K}}{2} \left[\frac{\langle U_{\delta} \rangle}{u^*} - \frac{1}{\kappa} \ln \left(\frac{\delta - d}{z_0} \right) \right]$$
(24)

where Φ_{δ} is the value of the cumulative distribution function at δ , typically near unity.

3.2. Morphometric model calibration from ARP estimates (Stage II)

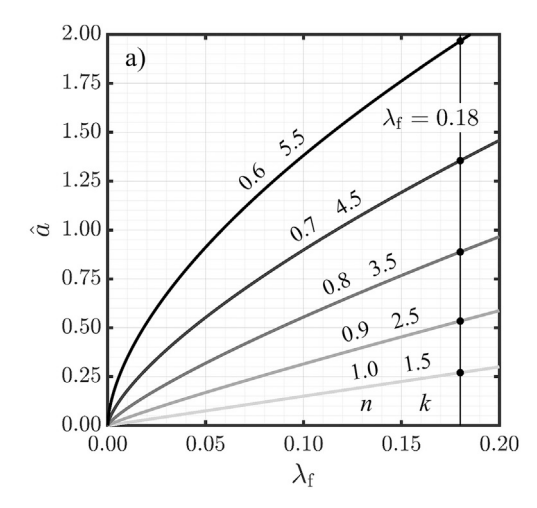
After ARP estimates are obtained from velocity profile data (following the steps in Section 3.1) through the full range of λ_f for several element height configurations, morphometric modeling is applied to predict ARPs for all roughness element heights. The output of Stage II is the functional relationship by which a BLWT modeler can adjust the element height to achieve user-specified ARPs for a given geometric scale.

3.2.1. Attenuation coefficient (a)

Following Macdonald (2000), the morphometric relationship to the UCL U profile shape is obtained by linking λ_f to a:

$$\hat{a} = k\lambda_{\rm f}^{\ n} \tag{25}$$

where k is a scaling factor and n is an exponent on the order of unity—introduced here to accommodate nonlinearity in the model for the range of $\lambda_{\rm f}$ —and the hat operator (^) indicates a model prediction. Fig. 3a shows the effect of tuning parameter adjustments on Eq. (25) for values ranging from n=0.6–1.0 and k=1.5–5.5. The resulting UCL U profile shape modification for each iteration of the morphometric model curve at a single frontal area density ($\lambda_{\rm f}=0.18$) is shown in Fig. 3b—presented in the dimensionless form U/U_h and z/h. In general, higher values of a—produced by lower values of n and higher values of k and k-increase k-profile curvature.



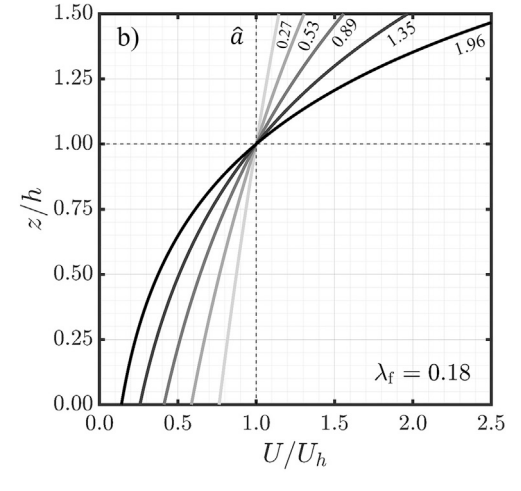


Fig. 3. a) Variation of \hat{a} with λ_f for the proposed model. b) Normalized *U* profiles for each iteration of the proposed model at $\lambda_f = 0.18$.

3.2.2. Zero-plane displacement height (\hat{d})

Analytical evaluation of the COP theorem formulated in Eq. (18) from $0 < z \le h$ —with the exponential mean velocity profile of Eq. (1)—for single-height rectangular-prism roughness leads to

$$\frac{\widehat{d}}{h} = \alpha \left(\frac{1}{1 - \exp(-2\widehat{a})} - \frac{1}{2\widehat{a}} \right) \tag{26}$$

This expression is evaluated after \hat{a} in Eq. (25) is calibrated from the ARP estimates. Fig. 4a depicts the variation of \hat{d}/h with $\lambda_{\rm f}$ for the range of \hat{a} presented in Fig. 3 in conjunction with $\alpha=0.4$ –1.0. The resulting log law vertical displacement is shown in Fig. 4b with profiles for a single frontal area density ($\lambda_{\rm f}=0.18$). In general, larger \hat{a} and α values produce larger \hat{d}/h values.

3.2.3. Roughness length (\hat{z}_0)

The roughness length is obtained from Macdonald et al. (1998a), which derived morphometric relationships from fundamental principles assuming negligible inter-element wake interference and a logarithmic approach flow U profile. The relationship between λ_f , \hat{d} , and \hat{z}_0 takes the form:

$$\frac{\widehat{z}_0}{h} = \left(1 - \frac{\widehat{d}}{h}\right) \exp\left[-\left(0.5\beta \frac{C_D}{\kappa^2} \left(1 - \frac{\widehat{d}}{h}\right) \lambda_f\right)^{-0.5}\right]$$
(27)

where β is a sheltering effect factor—calibrated from experimental data—that incorporates the drag correction factors $k_s, k_1, k_l, k_\theta, k_r$

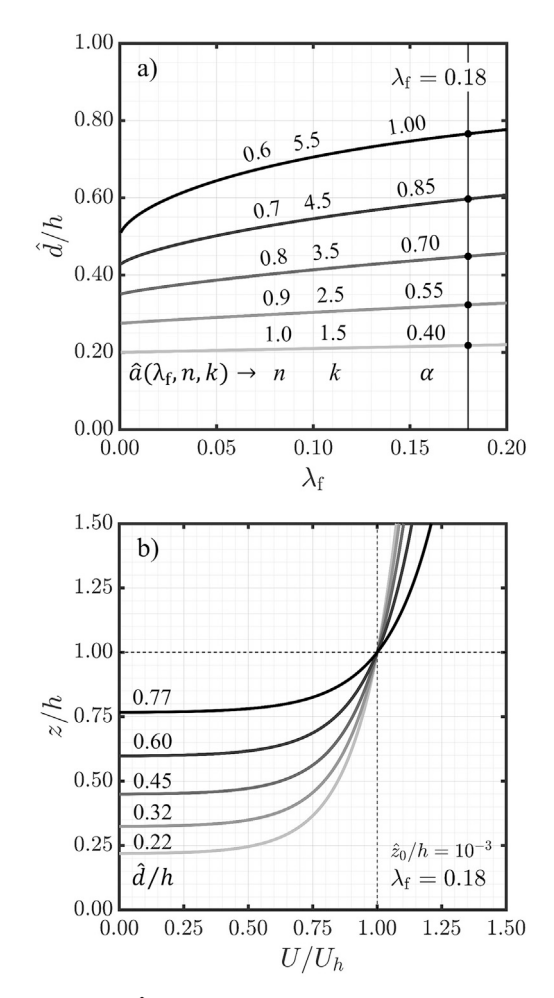


Fig. 4. a) Variation of \widehat{d}/h with λ_f for the analytical COP model for $\widehat{z}_0/h = 10^{-3}$ to isolate the effect of d on the logarithmic profile. b) Normalized U profiles for $\lambda_f = 0.18$ and $\widehat{z}_0/h = 10^{-3}$.

described in ESDU 80003 (1980) to modify the obstacle drag coefficient C_D . β accounts for modifications in drag by incorporating the correction factors into a single multiplicative parameter (Macdonald et al., 1998a). Fig. 5a shows the effect of tuning parameter adjustments on Eq. (27) for values ranging from $\beta=0.10-1.00$ and $\hat{d}/h=0$ for all cases to remove the vertical displacement effect on the log profile. Resulting changes in log law curvature are shown in Fig. 5b with profiles presented in the dimensionless form U/U_h and z/h for each iteration of the morphometric model curve at a single frontal area density ($\lambda_f=0.18$). In general, higher β values produce larger \hat{z}_0/h values and increase U profile curvature.

3.2.4. Shear velocity (\widehat{u}_*)

Finally, the shear velocity is obtained by imposing mean velocity continuity between the exponential and logarithmic profiles at z=h (Yang et al., 2016). The normalized shear velocity \hat{u}_*/U_h for a given h is determined from rearranging Eq. (2) as follows:

$$\frac{\widehat{u}_*}{U_h} = \left[\frac{1}{\kappa} \ln \left(\frac{h - \widehat{d}}{\widehat{z}_0} \right) \right]^{-1} = \left[\frac{1}{\kappa} \ln \left(\frac{1 - \widehat{d}/h}{\widehat{z}_0/h} \right) \right]^{-1}$$
(28)

where \widehat{d}/h and \widehat{z}_0/h are normalized model ARPs evaluated in Eq. (26) and Eq. (27), respectively. Here, no tuning parameter is required, since Eq. (28) will match estimated ARPs from Eq. (19) provided all previous steps are followed.

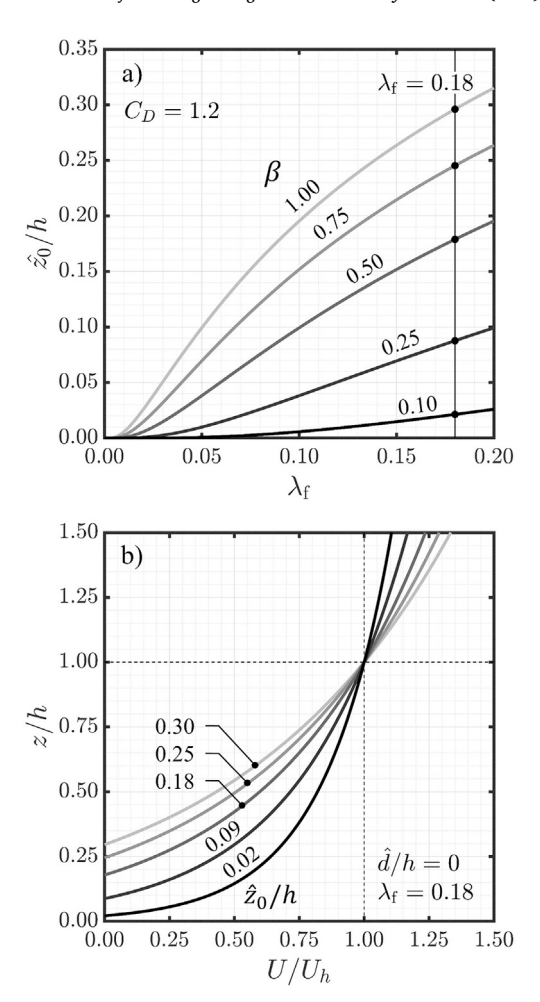


Fig. 5. a) Variation of \hat{z}_0/h with λ_f for the Macdonald et al. (1998a) model. b) Normalized U profiles for each iteration of the model at $\lambda_f=0.18$ and $\hat{d}/h=0$.

4. Experimental configuration

Data collection was carried out in the BLWT located at the University of Florida's Experimental Facility (UFEF), which is part of the National Science Foundation's (NSF) Natural Hazards Engineering Research Infrastructure (NHERI) program. The BLWT at UF is a long-fetch lowspeed open circuit tunnel with dimensions of 6 m W x 3 m H x 38 m L. The wind tunnel configuration is shown in Fig. 6 with right-handed Cartesian spatial coordinate system (x, y, z) indicated. The along-wind origin (x = z)0 mm) is located immediately downwind of the fan bank. Eight Aerovent 54D5 VJ vaneaxial fans driven by 75 hp (56 kW) AC induction motors generate air flow in the tunnel. Ambient intake air is pre-conditioned by a screen and honeycomb system to reduce fan-generated turbulence and ensure horizontal homogeneity of the velocity profile before entering the development section of the wind tunnel. The wind tunnel ceiling pitch is manually adjustable to produce approximately ZPG flows $(\partial P/\partial x \cong 0)$ along the length of the development and test sections. This condition was confirmed prior to testing by an array of wall-mounted static tube and differential pressure transducer assemblies stationed along the length of the tunnel.

4.1. Automated terrain generator (Terraformer)

The upwind terrain surface roughness was controlled by the Terraformer, a 62×18 array of 1116 stepper motor assemblies (Fig. 7) that translate and rotate roughness elements to control height and orientation from 0 to 160 mm and 0–360°, respectively (Fernández-Cabán and

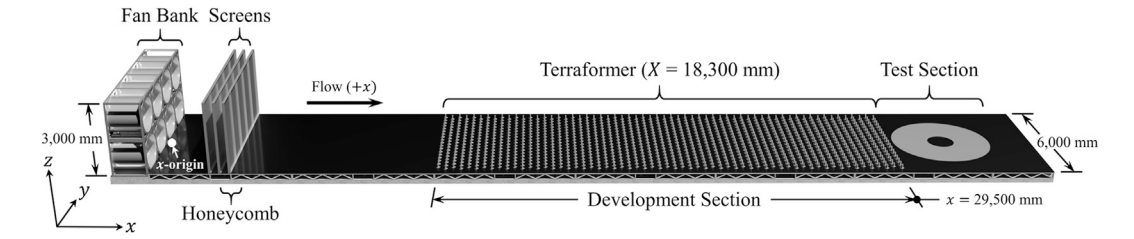


Fig. 6. Diagram of the BLWT at UF's NHERI experimental facility.

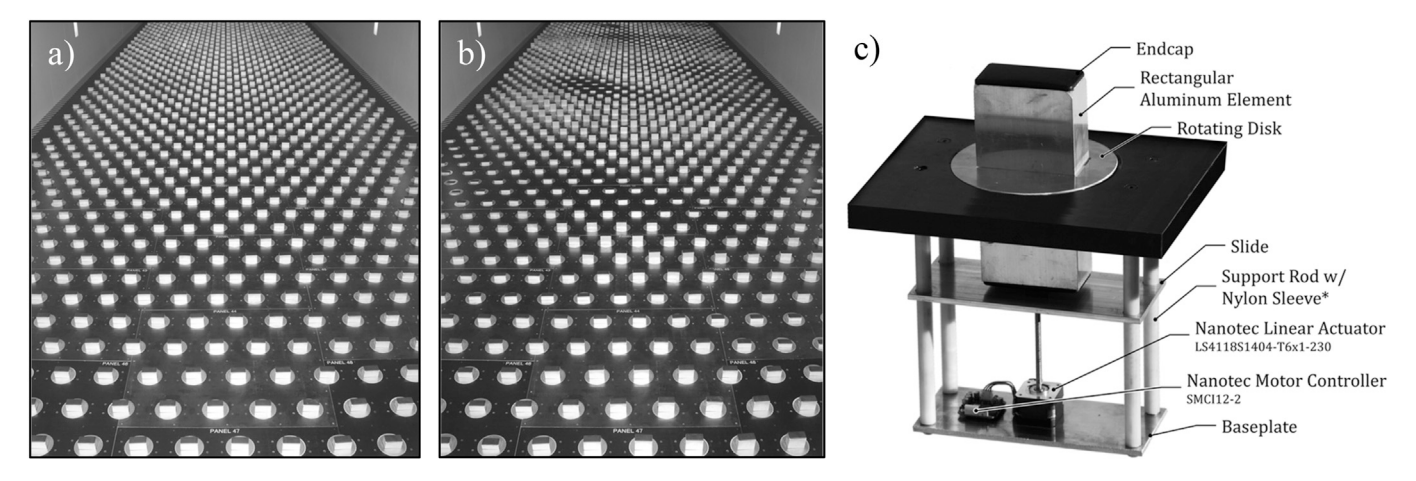


Fig. 7. a) Homogeneous array of roughness elements. b) Heterogeneous array of roughness elements. c) Rectangular aluminum roughness element and stepper motor assembly.

Masters, 2017). Each roughness element assembly consists of a linear actuator that both changes the height and orientation using a threaded rod that spins the element while only gradually changing the height

(Fig. 7c). Each element has nominal dimensions of 102 mm \times 51 mm (interchangeable as L_x or L_y) and a maximum actuated height of 160 mm, yielding a range of drag coefficients from 0.97 to 1.21, approximately.

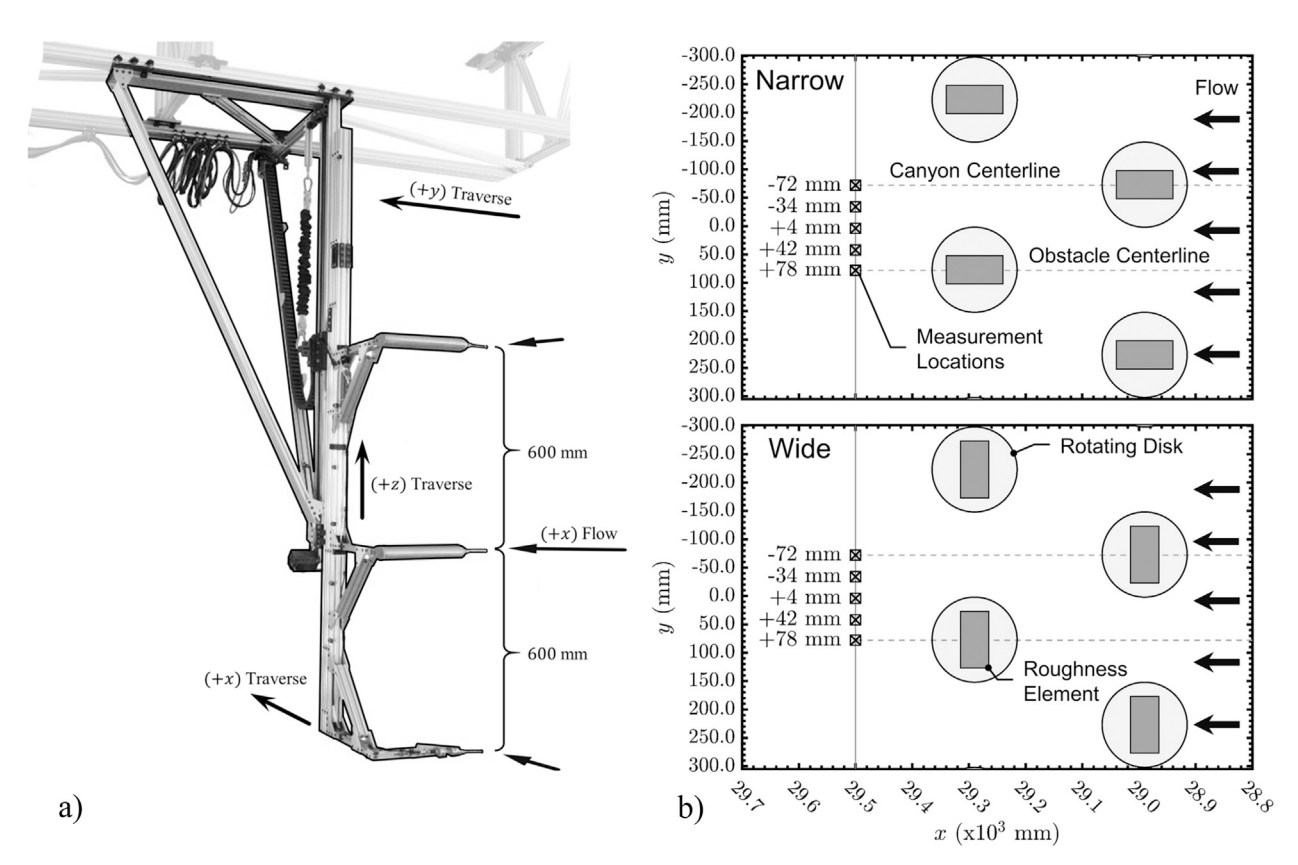


Fig. 8. a) Automated instrument gantry with three Cobra Velocity Probes. b) Plan view of narrow and wide element orientations with lateral measurement locations.

The roughness element grid is divided into 48 floor panels of 20 and 26 element groups with independent 24 VDC power and RS-485 communication busses. Each panel is modular and consists of surface-mounted roughness element assemblies and integrated wiring harnesses for power and signal distribution. This system can configure frontal areas ranging from a minimum of 0 mm² to a maximum of 16,256 mm² (i.e., $0 \le \lambda_f \le 0.18$). The roughness elements are spaced 300 mm apart in both the along-wind D_x and across-wind D_y dimensions in a staggered pattern with a fixed $\lambda_p = 0.058$, and the fetch length X extends nominally for 18,300 mm along the tunnel development section.

4.2. Velocity measurement

Velocity data were measured at the end of the development section (i.e., immediately downwind of the last row of roughness elements) using an automated multi-degree-of-freedom instrument gantry shown in Fig. 8a. This system is capable of traversing laterally and vertically nearly the entire width and height of the development section. The vertical arm was configured with three velocity probe holders equally spaced at 600 mm and was fitted with a pressure manifold to supply a stable atmospheric reference to each probe position.

The instrument gantry was equipped with three fast-response four-

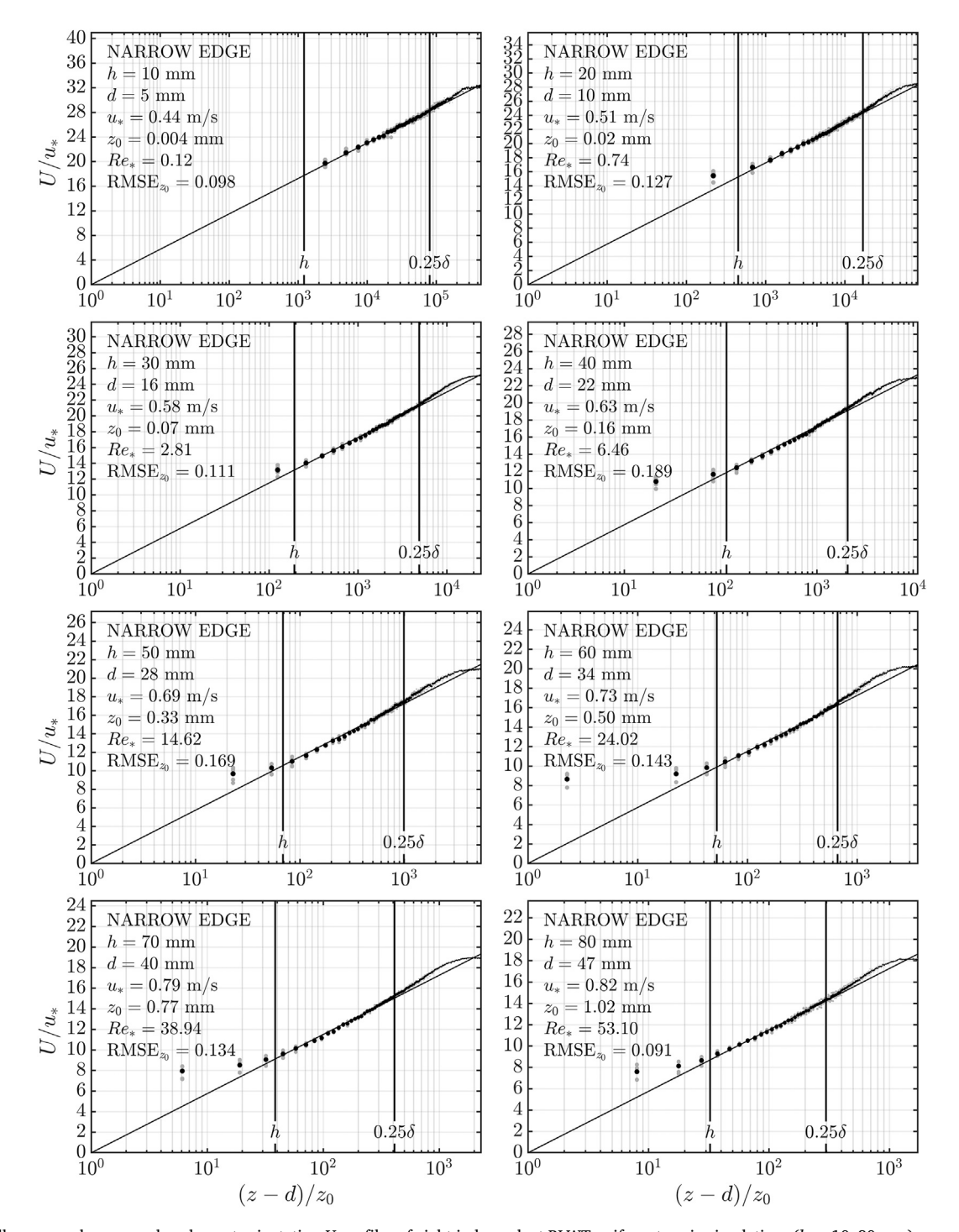


Fig. 9. Spatially-averaged narrow edge element orientation U profiles of eight independent BLWT uniform terrain simulations (h = 10–80 mm) measured at location x = 29,500 mm.

hole Turbulent Flow Instrumentation (TFI) Series 100 Cobra Velocity Probes that measure u, v, and w velocity components and static pressure within a $\pm 45^{\circ}$ acceptance cone. Performance characteristics include a maximum frequency response of 2 kHz, a 2–65 m/s sensing range, and a turbulence intensity I_u measurement range from 0 to 30% with a capability of >30%—albeit with decreased accuracy. The probes are accurate to a velocity of ± 0.3 m/s, and pitch and yaw angle measurements are accurate to $\pm 1.0^{\circ}$.

Test section air temperature, humidity, and barometric pressure were measured using a surface-mounted Omega iBTHX sensor centrally located on the ceiling above the test section (i.e., in the immediate

vicinity of all measurement locations). Measurements were taken periodically and supplied to the TFI software to accurately compensate for diurnal fluctuations in air density and atmospheric pressure.

A series of 33 experiments were performed over unique grid arrangements ranging from X/h=114–1830 and $\delta/h=8.4$ –139, which represent typical values for wind tunnel studies of urban BLs (Cheng et al., 2007). The roughness elements were uniformly actuated from h=10–160 mm in 10 mm increments for both wide and narrow element orientations. The flush floor configuration (h=0 mm) was also investigated. High resolution velocity profiles were measured for each element grid configuration at the end of the development section (i.e.,

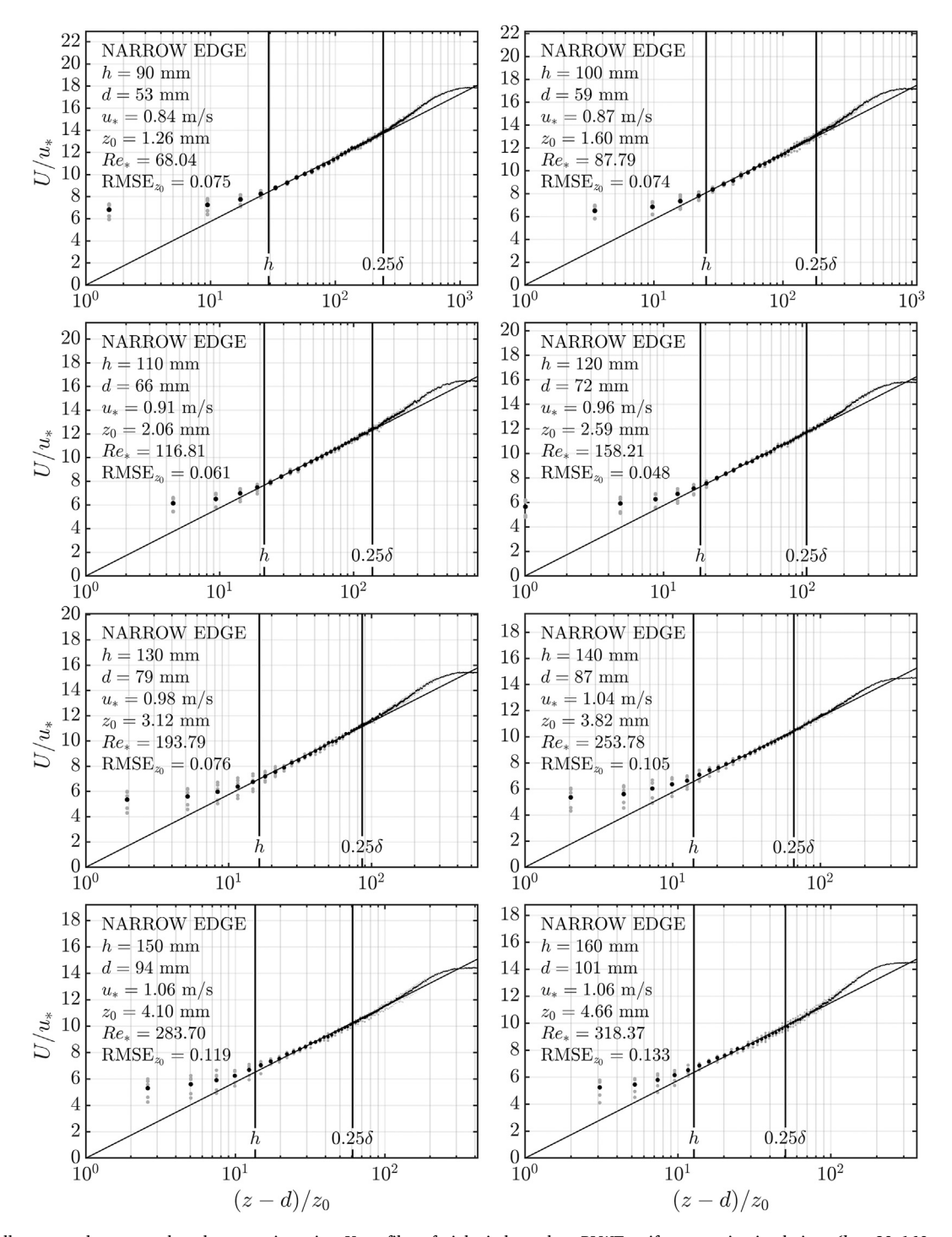


Fig. 10. Spatially-averaged narrow edge element orientation U profiles of eight independent BLWT uniform terrain simulations ($h = 90{\text -}160 \text{ mm}$) measured at location $x = 29{,}500 \text{ mm}$.

immediately behind the last row of roughness elements—x=29,500 mm) near the wind tunnel centerline. This measurement station was selected to fully characterize the BL profiles as they impinge on the test section turntable (see Fig. 6). Point measurements were taken for 30 s and sampled at 1250 Hz. Vertical traverses were executed from z=5-1805 mm in 10 mm increments at five lateral positions y (mm) = (-72, -34, 4, 42, 78) from the obstacle centerline to adjacent canyon centerline (see Fig. 8b).

In all tests, the vaneaxial fans were driven at 1050 RPM, with a ± 5 RPM observed variation for all testing conducted in this study, producing a free stream velocity of approximately 14.5 m/s for the flush element

configuration (i.e., minimum system resistance). Reynolds number effects (i.e., varied freestream velocities) were not investigated.

4.3. Data processing

Turbulent Flow Instruments (TFI) Cobra Probe data were low-pass filtered using a 3rd order Butterworth filter with a cut-off frequency of 200 Hz. Instantaneous velocity measurements outside of the acceptance cone—detected by TFI software—were resampled using linear interpolation to fill gaps in the velocity records. Such occurrences were only observed within the UCL because of the elevated levels of turbulence and

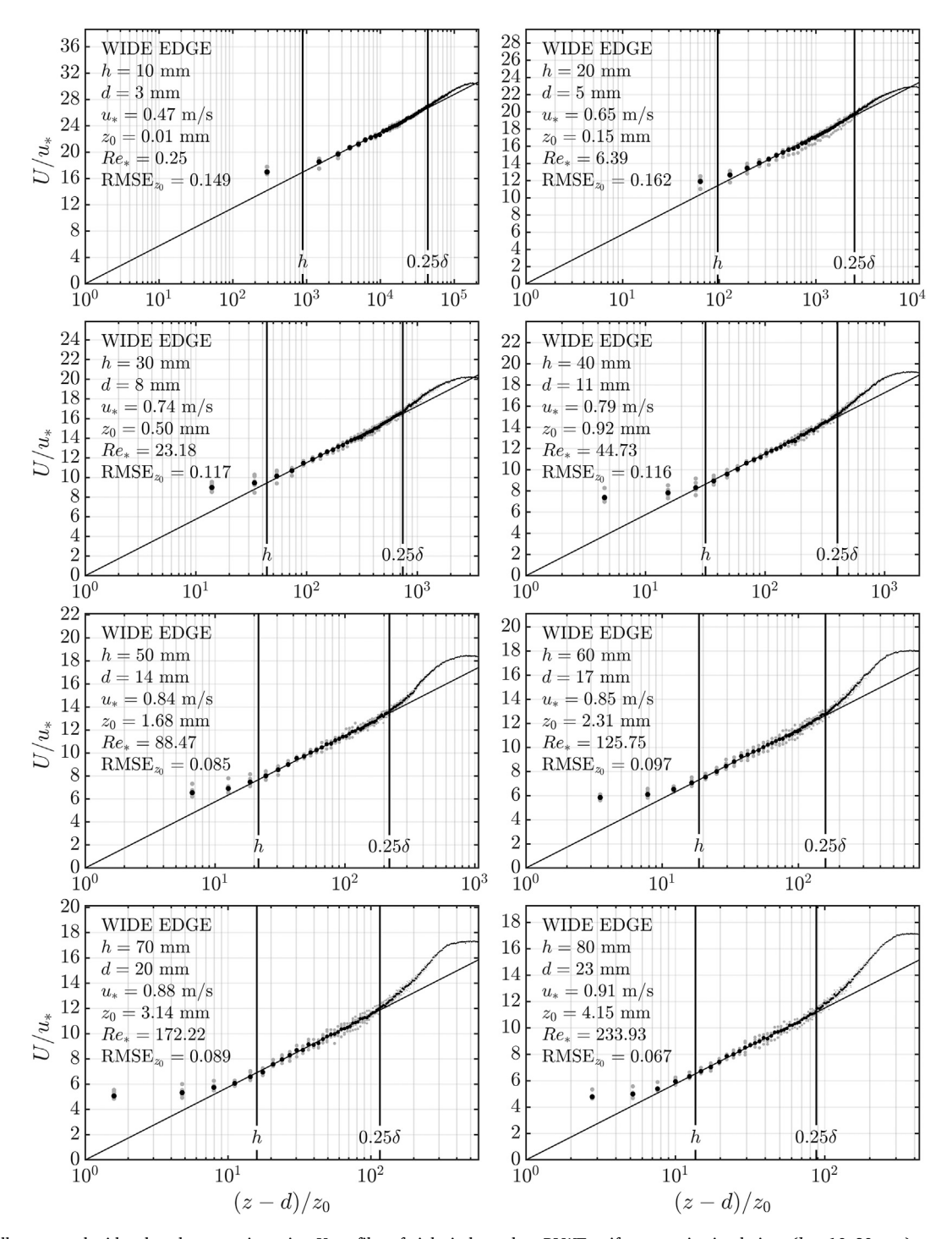


Fig. 11. Spatially-averaged wide edge element orientation U profiles of eight independent BLWT uniform terrain simulations (h = 10–80 mm) measured at location x = 29,500 mm.

increased rates of flow reversal. The highest rate of data loss occurred near the tunnel surface (z=5 mm) for all element configurations as expected. The minimum data acceptance value recorded was 61%, measured near the leeward roughness element separated flow region (y=42 mm). All measurements collected above the canopy height z>h experienced minimal data loss ($\leq 2\%$).

Each U profile was obtained from spatially-averaged measurements of five profiles across the width of the tunnel following the recommendation of Macdonald et al. (1998b):

$$\langle U \rangle(z) = \frac{1}{4} \left[0.5 U_{y_1}(z) + U_{y_2}(z) + U_{y_3}(z) + U_{y_4}(z) + 0.5 U_{y_5}(z) \right]$$
 (29)

where U_{y_i} is the mean velocity at each *y*-position. Spatial averaging of all statistics in this study follows the same weighting shown in Eq. (29).

5. Results and discussion

5.1. Characterization of the mean flow structure

Semi-logarithmic profiles of longitudinal mean velocity for narrow

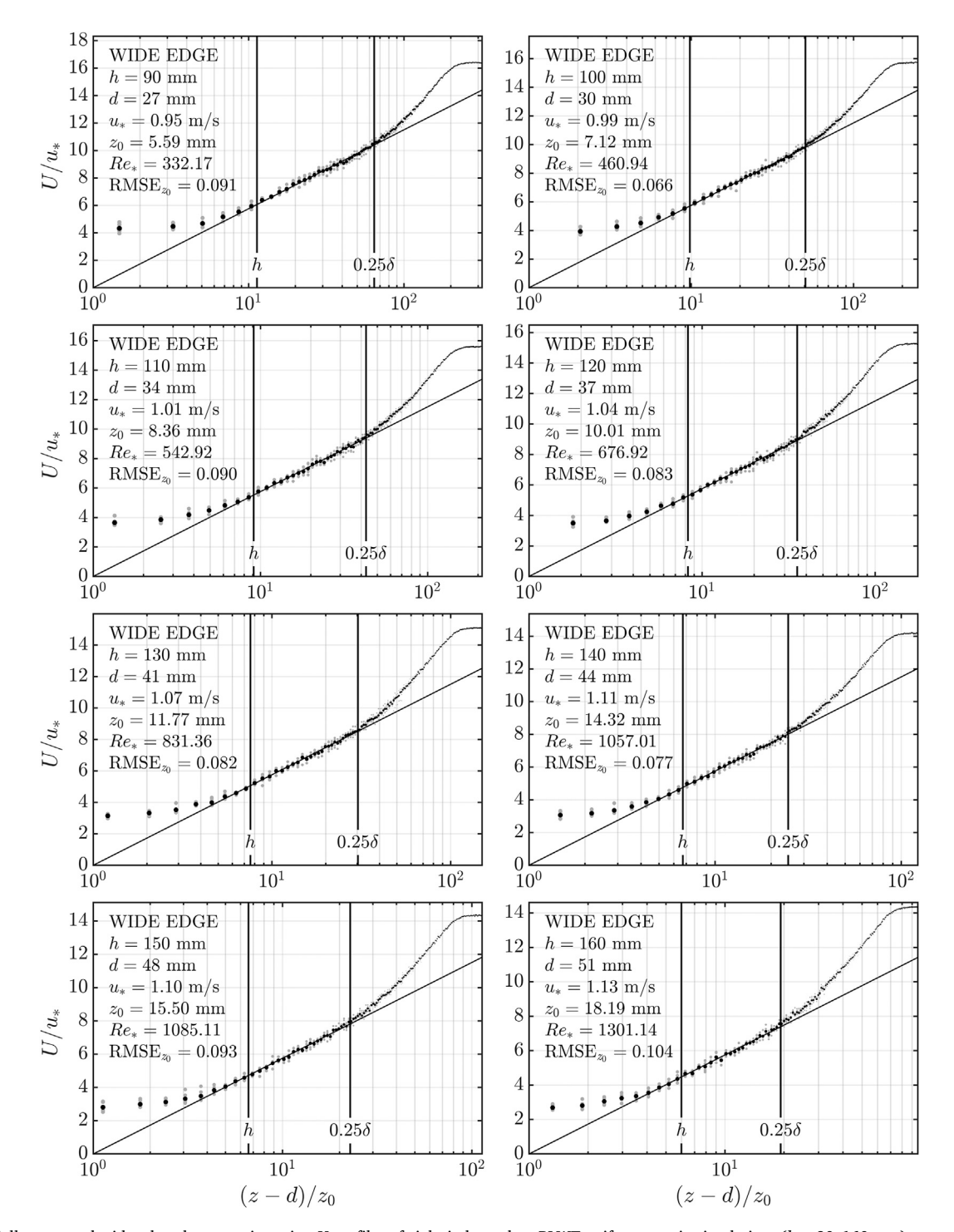


Fig. 12. Spatially-averaged wide edge element orientation U profiles of eight independent BLWT uniform terrain simulations (h = 90-160 mm) measured at location x = 29,500 mm.

Table 2ARPs and other BL characteristics for the narrow edge windward element orientation.

h (mm)	λ _f (%)	X/h	δ/h	<i>u</i> ∗ (m/s)	u_*/U_h	u_*/U_δ	d (mm)	d/h	z ₀ (mm)	z_0/h	а	П
0	0.00		_	0.37	_	0.025	0	_	0.00034	_	_	0.19
10	0.56	1830	132	0.44	0.05	0.031	5	0.51	0.004	0.0004	0.06	0.08
20	1.13	915	75	0.51	0.06	0.035	10	0.51	0.022	0.0011	0.11	0.09
30	1.69	610	50	0.58	0.07	0.040	16	0.53	0.074	0.0025	0.18	0.04
40	2.26	458	36	0.63	0.08	0.044	22	0.54	0.16	0.0040	0.26	0.03
50	2.82	366	28	0.69	0.09	0.048	28	0.55	0.33	0.0065	0.32	0.01
60	3.39	305	24	0.73	0.10	0.050	34	0.56	0.50	0.0083	0.37	0.06
70	3.95	261	20	0.79	0.11	0.053	40	0.58	0.77	0.0110	0.44	0.04
80	4.52	229	18	0.82	0.11	0.055	47	0.59	1.02	0.0128	0.51	0.03
90	5.08	203	16	0.84	0.12	0.056	53	0.59	1.26	0.0140	0.55	0.06
100	5.64	183	14	0.87	0.12	0.058	59	0.59	1.60	0.0160	0.59	0.06
110	6.21	166	13	0.91	0.13	0.061	66	0.60	2.06	0.0187	0.63	0.05
120	6.77	153	12	0.96	0.14	0.063	72	0.60	2.59	0.0216	0.66	0.04
130	7.34	141	11	0.98	0.14	0.065	79	0.61	3.12	0.0240	0.70	0.06
140	7.90	131	10	1.04	0.15	0.069	87	0.62	3.82	0.0273	0.75	0.00
150	8.47	122	9	1.06	0.15	0.070	94	0.63	4.10	0.0273	0.82	0.00
160	9.03	114	8	1.06	0.15	0.069	101	0.63	4.66	0.0291	0.83	0.10

and wide edge roughness element configurations—measured at x =29,500 mm-are shown in Figs. 9-12. ARP estimates obtained from spatially-averaged velocity data in the UCL (d estimates) and ISL (u* and z_0 estimates) are also presented. Measured mean velocity data at the five lateral positions are shown in gray, while black markers depict spatiallyaveraged data generated by Eq. (29). Following Cheng et al. (2007), Eq. (2) was fitted to each profile from $h \le z \le 0.25\delta$. The profiles are presented in the dimensionless form U/u_* and $(z-d)/z_0$ so that the slope of the fits equal $1/\kappa$ (i.e., 2.5). In general, measured profiles for both the narrow and wide element orientations show a strong match to the log law in the ISL-indicated by RMSE_{z0} values calculated using Eq. (20). In addition, Type A evaluations of standard uncertainty calculated from the adjacent mean flow profiles were between 0.01 and 0.18 m/s, with higher values observed near the element heights in all cases (e.g., 0.13 m/s for h = 160 mm wide edge). Above and below the ISL, the measured profiles depart from the log law, as expected. For lower element heights, the RSL is not pronounced. For higher element heights (Figs. 10 and 12), data in the RSL deviate significantly from the log progression.

Tables 2 and 3 summarize BL characteristics, surface morphometry, and estimated ARPs of all experiments conducted for the narrow and wide roughness element orientations, respectively. For element configurations with lower $\lambda_{\rm f}$ values, measurements of \overrightarrow{u} \overrightarrow{w} were found to vary with height in the ISL, so u_* was obtained from the RSSPE to the zeroplane level (Section 3.1.4), which Cheng et al. (2007) has shown to be consistent with surface drag measurements. The two element orientations display a systematic progression in d, u_* , and z_0 with increasing h. For the full range of h, the wide edge case consistently generates larger z_0

values than the narrow case. For instance, the wide edge case generates a z_0 nearly four times larger than the narrow edge case for h=160 mm. However, these two roughness configurations exhibit similar u^* values, where the wide case shows only a 5.6% increase over the narrow case. For the same h, reported values of d are nearly double for the narrow case compared to the wide case, where d(h=160 mm) is 61.3% and 31.3% of h. The flow is aerodynamically fully-rough for all roughness grid configurations of $h\geq 20$ mm wide and $h\geq 30$ mm narrow, where $2.81\leq Re^*\leq 1301.1$ —calculated from ARP estimates and ν determined from measured test section air properties.

Values of Π from ~ 0 to 0.64, which are difficult to estimate and highly sensitive to the other ARPs (Castro, 2007), were obtained using Eq. (24) and shown in Tables 2 and 3. Some evidence suggests that Π is insensitive to grid roughness characteristics if $\delta/h > 5$ and $\partial P/\partial x = 0$ in the fully-rough regime (Castro, 2007), so variation in the wake strength through the range of h indicates that high FST levels and/or non-zero longitudinal pressure gradients—a consequence of incrementally increasing grid roughness over the course of experiments-may have modified the BL structure. For ZPG flows at high Reynolds numbers, Coles (1956) initially proposed $\Pi = 0.55$ and later provided $\Pi = 0.62$ as an asymptotic wake strength value (Coles, 1987). Tani (1987) obtained values of Π ranging from 0.4 to 0.7, similar to values later obtained by Krogstad et al. (1992). This range of Π is consistent with the wide edge element configurations from 80 mm $\leq h \leq$ 160 mm, where the flow is aerodynamically fully-rough and the individual measured $\tau_{R_{mea}}$ profiles are near-constant with height in the ISL (e.g., Fig. 15b). This indirectly indicates that approximately ZPG flows were achieved for those element

Table 3ARPs and other BL characteristics for the wide edge element orientation.

h (mm)	λ_{f} (%)	X/h	δ/h	<i>u</i> ∗ (m/s)	u_*/U_h	u_*/U_δ	d (mm)	d/h	z_0 (mm)	z_0/h	а	П
0	0.00		_	0.37	_	0.025	0	_	0.00034	_	_	0.19
10	1.13	1830	149	0.47	0.06	0.033	3	0.26	0.01	0.0008	0.07	0.04
20	2.26	915	78	0.65	0.08	0.044	5	0.26	0.15	0.0077	0.14	0.00
30	3.39	610	51	0.74	0.10	0.050	8	0.27	0.50	0.0168	0.20	0.03
40	4.52	458	38	0.79	0.12	0.052	11	0.27	0.92	0.0230	0.25	0.13
50	5.64	366	31	0.84	0.13	0.054	14	0.28	1.68	0.0335	0.33	0.27
60	6.77	305	26	0.85	0.14	0.056	17	0.28	2.31	0.0386	0.40	0.36
70	7.90	261	22	0.88	0.15	0.058	20	0.29	3.14	0.0449	0.45	0.37
80	9.03	229	19	0.91	0.15	0.058	23	0.29	4.15	0.0518	0.55	0.47
90	10.16	203	17	0.95	0.16	0.061	27	0.30	5.59	0.0621	0.61	0.48
100	11.29	183	16	0.99	0.17	0.064	30	0.30	7.12	0.0712	0.64	0.46
110	12.42	166	14	1.01	0.18	0.064	34	0.31	8.36	0.0760	0.70	0.51
120	13.55	153	13	1.04	0.19	0.065	37	0.31	10.01	0.0835	0.72	0.53
130	14.68	141	12	1.07	0.20	0.066	41	0.31	11.77	0.0906	0.80	0.57
140	15.80	131	11	1.11	0.21	0.070	44	0.31	14.32	0.1023	0.83	0.49
150	16.93	122	11	1.10	0.21	0.070	48	0.32	15.50	0.1033	0.86	0.56
160	18.06	114	10	1.13	0.22	0.070	51	0.32	18.19	0.1133	0.93	0.64

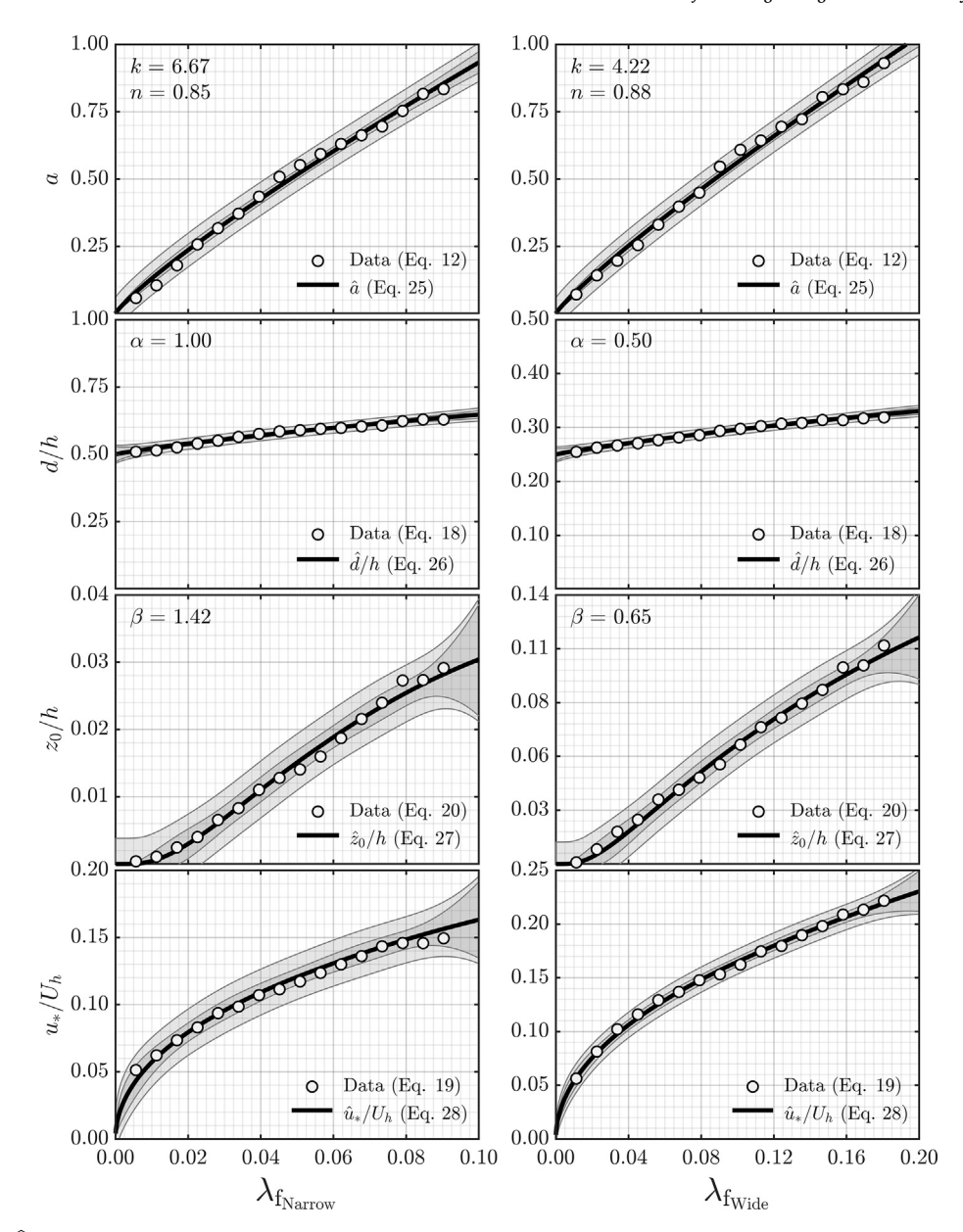


Fig. 13. Variation of \hat{a} , \hat{d}/h , \hat{z}_0/h , and \hat{u}_*/U_h with λ_f for narrow and wide Terraformer roughness grid configurations for the complete set of ARP estimates and morphometric model calibrations using the proposed framework (Section 3). Simultaneous functional intervals are shown in dark gray and simultaneous observational intervals are shown in light gray.

configurations (see Section 3.1.4). For the lowest element heights, the flow is not fully-rough, $\tau_{R_{xx}}$ profiles vary with height, and the FST level present in the UF BLWT may be suppressing the usual wake strength as observed by Thole and Bogard (1996). In the narrow edge case, Π is approximately zero through the full range of h, which is possibly attributable to high FST levels in conjunction with the lower drag produced. Nevertheless, the proposed procedure is able detect and account for wake strength variations observed in the range of configurations tested in this study.

5.2. ARP estimation and morphometric model calibration for all roughness element heights

Results of ARP estimates from velocity profile fitting (Section 3.1) and accompanying morphometric model calibrations (Section 3.2) for all experiments described in Section 4.2 are shown in Fig. 13. For each tuned morphometric model, upper and lower prediction bounds—with 95% confidence levels—are shown for both simultaneous functional (narrow

band) and simultaneous observational (wide band) prediction intervals to visualize the uncertainty of future predictions. The prediction intervals beyond the highest measured λ_f for \widehat{z}_0 and \widehat{u}_* increase rapidly, thus use of the models beyond the calibrated range is not recommended.

Tables 4 and 5 compare ARP estimation methods selected in this study to conventional alternatives. Raw COP estimates of d from Eq. (17) (i.e., $C_D = \text{constant}$) are compared with d estimates which incorporate approximate $C_D(z)$ functions (Mache, 2012; Tian, 2018) given similar area density parameters (e.g., λ_p and λ_f) for each element orientation to estimate α (Section 3.1.3). No drag correction (i.e., $\alpha=1$) is required for the narrow edge element orientation. However, a 50% reduction (i.e., $\alpha=0.5$) is required for the wide edge orientation. These results are compared to the 2P fit of Eq. (2), which show reasonable agreement. Similar agreement is observed when comparing the eddy diffusivity for momentum $K = -\langle \overrightarrow{u} \cdot \overrightarrow{w} \rangle / (\partial \langle U \rangle / \partial z) = \kappa u_* (z-d)$ in the ISL (Brunet et al., 1994), albeit with significant scatter through the range of λ_f . A primary benefit of using the COP method is the considerably lower variability

Table 4Narrow edge ARP estimation method comparisons.

h (mm)	λ_{f} (%)	(6) u∗ (m/s)			<i>d</i> (m	m)	z_0 (mm)	
		RSSPE*	Form drag	Peak	COP*	2P	1P*	2P
10	0.56	0.44	0.37	0.44	5	4	0.0040	0.0041
20	1.13	0.51	0.51	0.52	10	9	0.022	0.022
30	1.69	0.58	0.60	0.62	16	17	0.074	0.073
40	2.26	0.63	0.66	0.71	22	25	0.16	0.15
50	2.82	0.69	0.71	0.74	28	32	0.33	0.31
60	3.39	0.73	0.77	0.78	34	36	0.50	0.49
70	3.95	0.79	0.81	0.83	40	43	0.77	0.75
80	4.52	0.82	0.85	0.86	47	45	1.02	1.04
90	5.08	0.84	0.87	0.88	53	55	1.26	1.24
100	5.64	0.87	0.89	0.93	59	63	1.60	1.56
110	6.21	0.91	0.91	0.89	66	68	2.06	2.02
120	6.77	0.96	0.95	0.92	72	72	2.59	2.60
130	7.34	0.98	0.96	0.99	79	84	3.12	3.00
140	7.90	1.04	1.03	0.97	87	76	3.82	4.16
150	8.47	1.06	1.06	0.99	94	80	4.10	4.56
160	9.03	1.06	1.06	1.01	101	83	4.66	5.28

^{*} Applied in method

Table 5Wide edge ARP estimation method comparisons.

h (mm)	λ_{f} (%)	u_* (m/s)			<i>d</i> (m	m)	z_0 (mm)	
		RSSPE*	Form drag	Peak	COP*	2P	1P*	2P
10	1.13	0.47	0.37	0.42	3	2	0.0084	0.0085
20	2.26	0.65	0.77	0.68	5	2	0.15	0.16
30	3.39	0.74	0.87	0.80	8	7	0.50	0.51
40	4.52	0.79	0.94	0.97	11	14	0.92	0.90
50	5.64	0.84	0.98	1.02	14	13	1.68	1.68
60	6.77	0.85	1.01	1.07	17	18	2.31	2.30
70	7.90	0.88	1.03	1.10	20	22	3.14	3.10
80	9.03	0.91	1.06	1.16	23	23	4.15	4.15
90	10.16	0.95	1.07	1.14	27	22	5.59	5.74
100	11.29	0.99	1.08	1.20	30	27	7.12	7.25
110	12.42	1.01	1.11	1.27	34	32	8.36	8.43
120	13.55	1.04	1.12	1.27	37	39	10.01	9.90
130	14.68	1.07	1.12	1.25	41	41	11.77	11.74
140	15.80	1.11	1.13	1.34	44	43	14.32	14.39
150	16.93	1.10	1.13	1.24	48	56	15.50	14.82
160	18.06	1.13	1.13	1.31	51	59	18.13	17.46

Applied in method

Table 6Narrow edge ARP estimation and prediction comparisons.

h (mm)	λ _f (%)	C_D	a/\widehat{a}	d/\widehat{d}	z_0/\widehat{z}_0	u∗/û∗
10	0.56	0.97	0.73	0.99	8.48	1.19
20	1.13	0.97	0.73	0.98	1.67	1.03
30	1.69	0.97	0.88	0.98	1.23	1.00
40	2.26	0.97	0.98	0.99	1.03	0.99
50	2.82	0.97	1.00	1.00	1.08	1.01
60	3.39	0.97	1.00	1.01	0.99	0.98
70	3.95	0.98	1.03	1.01	1.03	0.99
80	4.52	0.98	1.07	1.01	0.98	0.97
90	5.08	0.99	1.05	1.01	0.92	0.97
100	5.64	0.99	1.04	1.00	0.92	0.97
110	6.21	1.00	1.01	0.99	0.96	0.98
120	6.77	1.01	0.99	0.99	1.00	0.99
130	7.34	1.02	0.97	0.99	1.03	1.00
140	7.90	1.03	0.99	1.00	1.09	0.99
150	8.47	1.04	1.01	1.00	1.03	0.96
160	9.03	1.05	0.97	0.99	1.04	0.96

.00 .99 .01 .98 .99

Table 7Wide edge ARP estimation and prediction comparisons.

h (mm)	λ _f (%)	C_D	a/\widehat{a}	d/\widehat{d}	z_0/\widehat{z}_0	u_*/\widehat{u}_*
10	1.13	1.19	0.86	0.99	1.41	1.00
20	2.26	1.19	0.93	1.00	1.63	1.03
30	3.39	1.19	0.90	0.99	1.45	1.06
40	4.52	1.19	0.91	0.99	1.16	1.04
50	5.64	1.19	0.97	0.99	1.18	1.04
60	6.77	1.19	0.99	0.99	1.04	1.01
70	7.90	1.19	0.98	0.99	0.99	1.02
80	9.03	1.19	1.06	1.01	0.97	0.99
90	10.16	1.19	1.07	1.00	1.01	0.99
100	11.29	1.19	1.03	1.01	1.04	1.01
110	12.42	1.19	1.02	1.01	1.01	1.00
120	13.55	1.20	0.99	1.00	1.01	1.01
130	14.68	1.20	1.02	1.00	1.02	1.01
140	15.80	1.20	0.99	0.99	1.08	1.03
150	16.93	1.21	0.97	0.99	1.03	1.02
160	18.06	1.21	0.99	0.98	1.07	1.02

compared to the alternatives. RSSPE estimates of u_* are compared to form drag calculations (see Section 3.1.3) and the peak values of $\tau_{R_{xx}}$ profiles. Agreement is shown between the methods, but with considerably higher

variability within each of the alternatives. The RSSPE procedure is found to accommodate near-constant stress ISL regions (e.g., Fig. 15b) in addition to regions with strong vertical stress gradients—common in

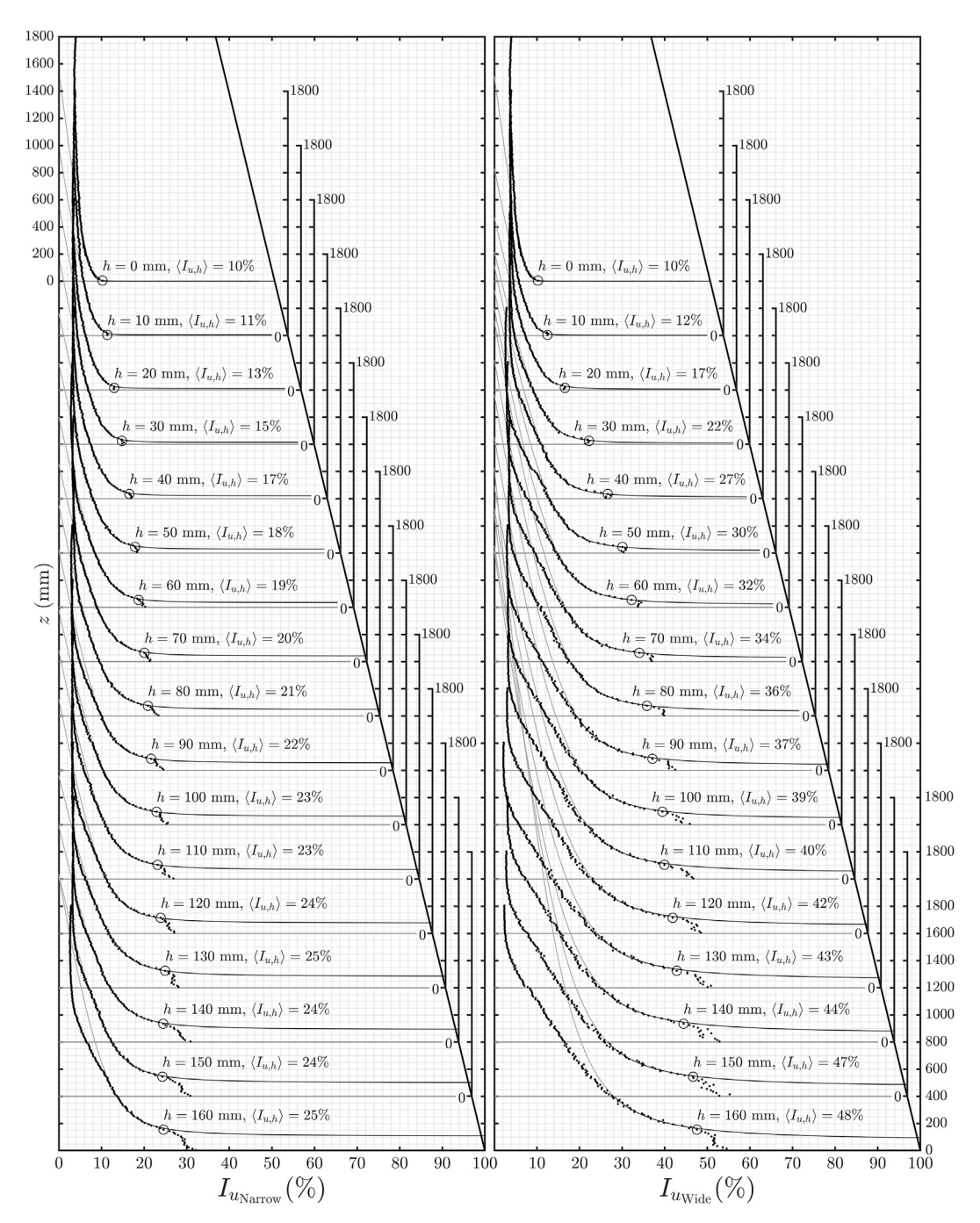


Fig. 14. Spatially-averaged longitudinal turbulence intensity $\langle I_u \rangle$ profiles for narrow and wide edge element orientations of 33 independent BLWT uniform terrain simulations (h = 0–160 mm) measured at location x = 29,500 mm \hat{I}_u is superimposed for all profiles.

BLWT simulations. Using estimates from the COP and RSSPE (d and u_s , respectively), the 1P fit of $\langle U \rangle$ profile data to Eq. (2) produces a clear monotonic trend of z_0 . Comparisons of 1P to 2P z_0 estimates show reasonable agreement. Further, estimates of z_0 are shown to be insensitive to moderate variations in the magnitude of d (e.g., <3.70% difference in z_0 for variation of \sim 13.6% in d for h=160 mm wide edge orientation).

Tables 6 and 7 compare predicted ARPs to estimated values using ratios. Morphometric model calibrations (Section 3.2) produce ARP predictions that closely match estimates after applying tuning parameter adjustments. Calibration of \widehat{a} produces good agreement with ARP estimates, with k=6.67,4.22 and n=0.85,0.88 for narrow edge and wide edge elements, respectively. The analytic COP model in Eq. (26) shows strong agreement to the ARP estimates in Eq. (18) provided drag

corrections found during ARP estimation are also applied. The Macdonald et al. (1998a) model for \widehat{z}_0 (see Eq. (27)) agrees well with estimates after applying cuboid C_D values from ESDU 80003 (1980) and sheltering effect factors of $\beta=1.42$ and $\beta=0.65$ for narrow and wide edge element orientations, respectively. Consider that $\beta>1$ in the narrow case is effectively an increase in C_D above the value for an isolated cuboid element (ESDU 80003, 1980). Macdonald et al. (1998b) indicates that there is no experimental justification for this result, although unexpected drag modifications may occur inside the shear layer for particular configurations of surface roughness. With predictions of \widehat{z}_0 and \widehat{d} , \widehat{u}^* is calculated using the rearranged log law presented in Eq. (28)—used to verify that the morphometric models and estimates remain in agreement. This model is not fitted to estimates independently (i.e., no

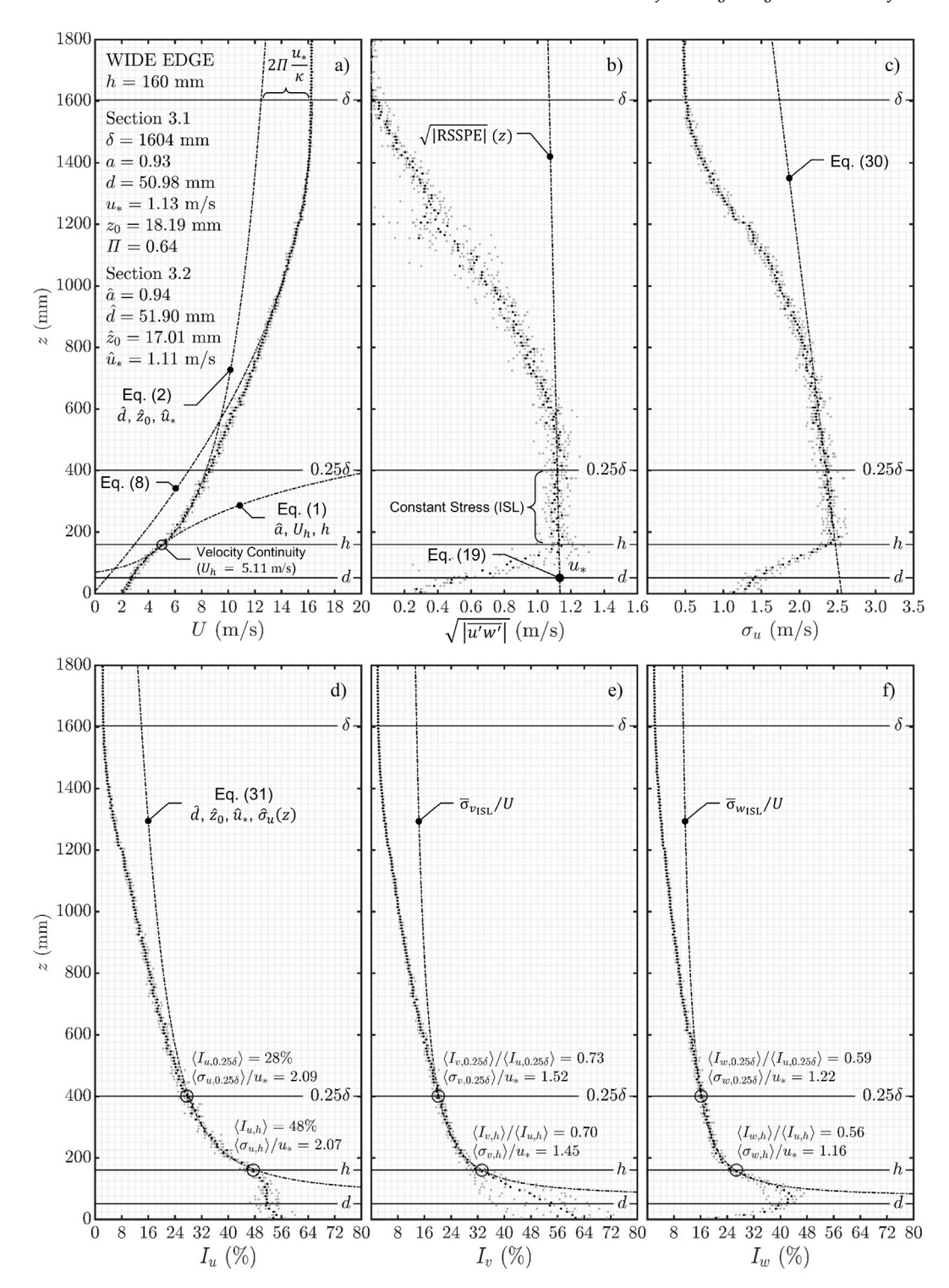


Fig. 15. Wide edge element (h = 160 mm) BL flow structure measured at location x = 29,500 mm. Gray markers are individual adjacent profiles and black markers are spatially-averaged data.

tuning parameters are employed), so matching in this final step increases confidence in the tuning process.

5.3. Extension to quantify the longitudinal turbulence intensity profile

Spatially-averaged longitudinal turbulence intensity $\langle I_u \rangle$ profiles—measured at x=29,500 mm—for all Terraformer configurations are depicted in Fig. 14. The left and right subplots correspond to narrow and wide edge roughness element orientations, respectively. Individual $\langle I_u \rangle$

profiles are monotonic and consistently trend from maximum values in the UCL to minimum values in the freestream with noticeable changes in curvature starting in the RSL. These inflection regions appear to coincide with roughness element heights indicating a change in turbulence structure. All $\langle I_u \rangle$ profiles converge to the FST level (i.e., $I_u \sim 3.5\%$) by approximately z=1605 mm, where the influence of the Terraformer on the approach flow vanishes.

A greater range of turbulence is achieved when elements are oriented in a wide edge orientation, showing higher turbulence levels near the tunnel floor (z < 400 mm) through the full range of h when compared to the narrow configuration. For instance, $\langle I_u \rangle (z=h)$ for the highest element height (i.e., h=160 mm) nearly doubles when reconfiguring the elements from a narrow to a wide edge windward orientation—i.e., $\langle I_u \rangle (z=h)=25\%$ and 48%, respectively.

An important observation from higher-order velocity profile data analysis is the presence of negative sloping near-linear vertical variations of longitudinal standard deviation σ_u in the ISL (e.g., Fig. 15c) for all Terraformer configurations—in contrast to the Monin-Obukhov similarity requirement of $\sigma_u/u^*=$ constant for purely mechanical turbulence in the neutrally-stratified atmospheric surface layer (Panofsky and Dutton, 1983; Högström, 1990). This finding is corroborated by other BLWT studies (Raupach, 1981; Raupach et al., 1991; Brunet et al., 1994) depicting $\langle \sigma_u \rangle$ profile variation with height in the ISL—reaching a peak near h and decreasing monotonically up to the freestream. As a consequence of the trend in σ_u with height, the wind tunnel BLs fail to meet this strict condition. However, the variation in most cases does not exceed $\sim 13\%$ through the depth of the ISL.

To systematically characterize the trend in σ_u , a simple linear fit can be applied:

$$\widehat{\sigma}_{u}(z) = \left(z - b_{\sigma_{u}}\right) / m_{\sigma_{u}} \tag{30}$$

where b_{σ_u} is the *z*-intercept and m_{σ_u} is the slope of the best fit line to the $\langle \sigma_u \rangle$ profile in the ISL. This profile model can be applied to more accurately predict the wind tunnel I_u profile generated by each measured configuration of the roughness grid, but is of limited utility since it is not a continuous morphometric solution.

If σ_u is assumed to be constant in the BLWT ISL—or if the σ_u profiles are assumed to increase with height as in ESDU 85020 (1985)—and a negative gradient exists in reality, errors between predicted I_u values and measurements may become significant. Even modest variations of σ_u/u^s with height may produce meaningful errors. From $I_u = \sigma_u/U$ (Panofsky and Dutton, 1983; Holmes, 2018), the morphometric turbulence intensity model is defined as:

$$\widehat{I}_{u}(z) = \frac{\widehat{\sigma}_{u}(z)\kappa}{\widehat{u}_{*}} \ln \left(\frac{z - \widehat{d}}{\widehat{z}_{0}}\right)^{-1}$$
(31)

where $\widehat{\sigma}_u(z)$ is the predicted longitudinal standard deviation profile as a function of height. This model matches turbulence intensities using the predicted ARPs of Section 3.2 (i.e., \widehat{z}_0 , \widehat{d} , and \widehat{u}^*) and the fit of Eq. (30) to each measured profile. In general, the \widehat{I}_u model of Eq. (31) shows excellent agreement with measured $\langle I_u \rangle$ data in the lower portion of the profiles (h < z < 400 mm) within the ISL (see Fig. 14). The model begins to deviate from measured $\langle I_u \rangle$ profiles at higher elevations (i.e., transition to outer wake layer) as expected.

5.4. A complete visualization of the framework

Fig. 15 visualizes the complete framework (Section 3) applied to a representative set of velocity profile data (i.e., h=160 mm wide edge orientation—x=29,500 mm) plotted on linear scales without normalization to represent real proportions of the BL structure. In addition, turbulence characteristics (i.e., I_u , I_v , I_w) are displayed in relation to the mean flow structure. All profile curve fits are applied to spatially-averaged data shown in black markers, with lateral profiles displayed in gray markers to reveal local flow variations in the UCL—clearly evident between the lateral profiles of I_v and I_w —and convergence to global conditions in the ISL. Divisions between distinct sublayers are shown to identify applicable ARP fitting regions.

In Fig. 15a, mean profiles generated using calibrated ARP predictions (Section 3.2) for Eq. (1) in the UCL (0 $< z \le h$) and Eq. (2) in the ISL ($h \le z \le 0.25\delta$) demonstrate strong agreement with $\langle U \rangle$ profile data. Velocity continuity between Eq. (1) and Eq. (2) at z=h—valid for spatially-averaged data—is imposed. Profile curve fits that initially produced

ARP estimates (Section 3.1) in these regions are omitted for clarity since there is essentially no difference between the estimated and predicted profiles (i.e., profiles overlap). The fit of Eq. (8) to the upper half of the $\langle U \rangle$ profile is also shown to demonstrate the estimation method for δ (Section 3.1.1). The majority of the wind tunnel profile consists of the outer wake layer—visible from $0.25\delta < z \le \delta$ —and the magnitude of $\langle U \rangle$ data deviation from Eq. (2) at $z = \delta$ is given by $2\Pi u^s/\kappa$. The $\langle U \rangle$ profile is effectively constant for $z > \delta$. ARP estimate and prediction values resulting from the framework are also reported.

Fig. 15b displays profiles of $\sqrt{|\overrightarrow{uw}|}$ data—increasing from the tunnel floor to h, remaining approximately constant with height in the ISL, decreasing in the outer layer, and effectively diminishing to zero in the freestream. Scatter among the adjacent profiles is high for these data, but clear trends remain visible in the distinct BL regions. The visualized RSSPE technique of Eq. (19) with the intersection point at the zero-plane level demonstrates the estimation of u_* (Section 3.1.4)—a method shown to be consistent with direct drag force measurements (Cheng et al., 2007). The resulting u_* estimate for this roughness configuration is nearly identical to the vertically averaged u_* data points in the ISL (i.e., the fit line is nearly vertical). However, this is not the case for all h since $\sqrt{|\overrightarrow{uw}|}$ profiles for low element heights exhibit a significant negative

 $\sqrt{|\vec{u}\cdot\vec{w}|}$ profiles for low element heights exhibit a significant negative vertical gradient $(\partial\sqrt{|\vec{u}\cdot\vec{w}|}/\partial z < 0)$.

Fig. 15c shows variations with height in the σ_u profile data. An abrupt shape change is visible between the UCL and ISL starting at approximately z=h, and the lateral profiles are almost completely linear through the ISL and into the outer layer, where σ_u transitions towards the freestream value. Beyond $z=\delta$, σ_u is nearly constant with height. Data in the ISL is fit using Eq. (30) to characterize the vertical trend of $\langle \sigma_u \rangle$.

Lastly, longitudinal (I_u) , lateral (I_v) , and vertical (I_w) turbulence intensity profile data and corresponding model profile curves are illustrated in Fig. 15d–f. Model \widehat{I}_u , \widehat{I}_v , and \widehat{I}_w profiles are generated from Eq. (31) using predicted ARP values—shown in Fig. 15a—in addition to $\widehat{\sigma}_u(z)$ from Eq. (30), vertically averaged ISL σ_v values, and vertically averaged ISL σ_w values, respectively. The model curves show strong matching despite no direct fitting to these data (i.e., fits were performed to $\langle U \rangle$ and $\langle \sigma_u \rangle$ data). Values of $\langle \sigma_u \rangle / u_v$, $\langle \sigma_v \rangle / u_v$, and $\langle \sigma_w \rangle / u_v$ —similar to those found by Raupach et al. (1986)—are shown at z=h and $z=0.25\delta$ to indicate variation with height for $\langle I_u \rangle$, $\langle I_v \rangle$, and $\langle I_w \rangle$ profiles, respectively. The turbulence ratios $\langle I_v \rangle / \langle I_u \rangle$ and $\langle I_w \rangle / \langle I_u \rangle$ are also shown at each height in Fig. 15e and f, respectively.

6. Conclusions

A two-stage framework to characterize BL mean flows was demonstrated via a comprehensive series of BLWT experiments coupled with a set of morphometric models—based on roughness grid geometry—to produce ARP predictions for the full range of achievable $\lambda_{\rm f}$ with minimal empirical calibration. In general, the calibrated morphometric models produce exceptional predictions of a, d, z_0 , and u_* for the family of homogeneous Terraformer configurations considered. Given the outcome of this investigation, the framework could prove to be a useful guideline for commissioning or verifying new or existing BLWT facilities.

In addition to the proposed framework, the study illustrates the efficacy of the Terraformer to investigate a wide-ranging and diverse group of upwind terrain conditions in a relatively short timeframe (e.g., ~ 50 min of combined setup time for all experiments compared to ~ 70 h for a traditional manual approach), thus eliminating the need for timeintensive iteration of development section configurations. The versatility of the Terraformer will also enable analysis of flow fields over complex non-uniform (i.e., heterogeneous) terrains through individual element height control. Future work will center on the generation of discrete random element fields based on stochastic simulation techniques (e.g., Masters and Gurley, 2003) from prescribed statistical distributions.

These heterogeneous element arrays will potentially permit modulation of higher order (e.g., turbulence) statistics of the approach flow for a given set of ARPs to attain desired full-scale mean and turbulence profiles representative of a target 3D terrain environment. Subsequent works will also entail the development of predictive models to relate the mechanical turbulence of the approach flow and the morphometric properties of heterogeneous terrains.

CRediT authorship contribution statement

R.A. Catarelli: Conceptualization, Methodology, Software, Formal analysis, Investigation, Data curation, Writing - original draft, Writing - review & editing, Visualization. P.L. Fernández-Cabán: Conceptualization, Software, Methodology, Resources, Writing - original draft, Writing - review & editing, Supervision. F.J. Masters: Conceptualization, Software, Methodology, Resources, Writing - original draft, Writing - review & editing, Supervision, Project administration, Funding acquisition. J.A. Bridge: Writing - review & editing, Supervision, Funding acquisition. K.R. Gurley: Resources, Writing - review & editing, Supervision, Funding acquisition. C.J. Matyas: Writing - review & editing, Supervision, Funding acquisition. Funding acquisition.

Declaration of competing interest

The authors declare that they have no known competing financial interests or personal relationships that could have appeared to influence the work reported in this paper.

Acknowledgements

Support for this research was provided by the National Science Foundation MRI program (CMMI-1428954) with additional support for experimentation through the NSF Natural Hazards Engineering Research Infrastructure (NHERI, CMMI-1520843). The authors also wish to recognize the Powell Structures and Materials Laboratory staff, with special thanks to Alex Esposito, Shelby Brothers, Eric Agostinelli, Kevin Stultz, Steve Schein, and Travis Cole for their invaluable contributions to instrument design, construction, and wind tunnel testing. Any opinions, findings, and conclusions or recommendations expressed in this paper are those of the authors and do not necessarily reflect the views of the sponsors, partners, and contributors.

References

- Barlow, J.B., Rae, W.H., Pope, A., 1999. Low-speed Wind Tunnel Testing. John wiley & sons.
- Bentham, T., Britter, R., 2003. Spatially-averaged flow within obstacle arrays. Atmos. Environ. 37 (15), 2037–2043.
- Böhm, M., Finnigan, J.J., Raupach, M.R., Hughes, D., 2013. Turbulence structure within and above a canopy of bluff elements. Boundary-Layer Meteorol. 146 (3), 393–419. Bottema, M., 1995. Parametization of aerodynamic roughness parameters in relation with air pollutant removal efficiency of streets. WIT Trans. Ecol. Environ. 10.
- Bottema, M., 1997. Urban roughness modelling in relation to pollutant dispersion. Atmos. Environ. 31 (18), 3059–3075.
- Brunet, Y., Finnigan, J.J., Raupach, M.R., 1994. A wind tunnel study of air flow in waving wheat: single-point velocity statistics. Boundary-Layer Meteorol. 70 (1–2), 95–132.
- Castro, I.P., 2017. Are urban-canopy velocity profiles exponential? Boundary-Layer Meteorol. 164 (3), 337–351.
- Castro, I.P., 2007. Rough-wall boundary layers: mean flow universality. J. Fluid Mech. 585, 469–485.
- Castro, I.P., Cheng, H., Reynolds, R., 2006. Turbulence over urban-type roughness: deductions from wind-tunnel measurements. Boundary-Layer Meteorol. 118 (1), 109–131.
- Cheng, H., Hayden, P., Robins, A.G., Castro, I.P., 2007. Flow over cube arrays of different packing densities. J. Wind Eng. Ind. Aerod. 95 (8), 715–740.
- Cionco, R.M., 1965. A mathematical model for air flow in a vegetative canopy. J. Appl. Meteorol. 4 (4), 517–522.
- Coceal, O., Belcher, S.E., 2004. A canopy model of mean winds through urban areas. Q. J. R. Meteorol. Soc. 130 (599), 1349–1372.
- Coceal, O., Thomas, T.G., Castro, I.P., Belcher, S.E., 2006. Mean flow and turbulence statistics over groups of urban-like cubical obstacles. Boundary-Layer Meteorol. 121 (3), 491–519.

- Coceal, O., Dobre, A., Thomas, T.G., Belcher, S.E., 2007. Structure of turbulent flow over regular arrays of cubical roughness. J. Fluid Mech. 589, 375–409.
- Coles, D., 1956. The law of the wake in the turbulent boundary layer. J. Fluid Mech. 1 (2), 191–226.
- Coles, D., 1987. Coherent structures in turbulent boundary layers. Perspectives in Turbulence Studies. Springer, Berlin, Heidelberg, pp. 93–114.
- Cook, N.J., 1978. Wind-tunnel simulation of the adiabatic atmospheric boundary layer by roughness, barrier and mixing-device methods. J. Wind Eng. Ind. Aerod. 3 (2–3), 157–176
- Counihan, J., 1969. An improved method of simulating an atmospheric boundary layer in a wind tunnel. Atmos. Environ. 3 (2), 197IN1201–200IN2214, 1967.
- De Bortoli, M.E., Natalini, B., Paluch, M.J., Natalini, M.B., 2002. Part-depth wind tunnel simulations of the atmospheric boundary layer. J. Wind Eng. Ind. Aerod. 90 (4–5), 281–291.
- ESDU 80003, 1980. Mean Fluid Forces and Moments on Rectangular Prisms: Surface-Mounted Structures in Turbulent Shear Flow. Engineering Sciences Data Unit.
- ESDU 85020, 1985. Characteristics of Atmospheric Turbulence Near the Ground: Part II: Single Point Data for Strong Winds (Neutral Atmosphere). Engineering Sciences Data Unit.
- Farell, C., Iyengar, A.K., 1999. Experiments on the wind tunnel simulation of atmospheric boundary layers. J. Wind Eng. Ind. Aerod. 79 (1), 11–35.
- Fernández-Cabán, P.L., Masters, F.J., 2017. Near surface wind longitudinal velocity positively skews with increasing aerodynamic roughness length. J. Wind Eng. Ind. Aerod. 169, 94–105.
- Finnigan, J., 2000. Turbulence in plant canopies. Annu. Rev. Fluid Mech. 32 (1), 519–571.
- Gartshore, I.S., De Croos, K.A., 1977. Roughness element geometry required for wind tunnel simulations of the atmospheric wind. J. Fluid Eng. 99 (3), 480–485.
- Grimmond, C.S.B., Oke, T.R., 1999. Aerodynamic properties of urban areas derived from analysis of surface form. J. Appl. Meteorol. 38 (9), 1262–1292.
- Guo, J., 1998. Turbulent Velocity Profiles in Clear Water and Sediment-Laden Flows. Doctoral dissertation, Colorado State University.
- Hancock, P.E., Bradshaw, P., 1983. The effect of free-stream turbulence on turbulent boundary layers. J. Fluid Eng. 105 (3), 284–289.
- Högström, U., 1990. Analysis of turbulence structure in the surface layer with a modified similarity formulation for near neutral conditions. J. Atmos. Sci. 47 (16), 1949–1972. Holmes, J.D., 2018. Wind Loading of Structures, CRC press.
- Hussain, M., Lee, B.E., 1980. A wind tunnel study of the mean pressure forces acting on large groups of low-rise buildings. J. Wind Eng. Ind. Aerod. 6 (3–4), 207–225.
- Iyengar, A.K., Farell, C., 2001. Experimental issues in atmospheric boundary layer simulations: roughness length and integral length scale determination. J. Wind Eng. Ind. Aerod. 89 (11–12), 1059–1080.
- Jackson, P.S., 1981. On the displacement height in the logarithmic velocity profile. J. Fluid Mech. 111, 15–25.
- Jiang, D., Jiang, W., Liu, H., Sun, J., 2008. Systematic influence of different building spacing, height and layout on mean wind and turbulent characteristics within and over urban building arrays. Wind Struct. 11 (4), 275–290.
- Jiménez, J., 2004. Turbulent flows over rough walls. Annu. Rev. Fluid Mech. 36, 173–196.
- Kanda, M., Moriizumi, T., 2009. Momentum and heat transfer over urban-like surfaces. Boundary-Layer Meteorol. 131 (3), 385–401.
- Karimpour, A., Kaye, N.B., Baratian-Ghorghi, Z., 2012. Modeling the neutrally stable atmospheric boundary layer for laboratory scale studies of the built environment. Build. Environ. 49, 203–211.
- Krogstad, P.Å., Antonia, R.A., Browne, L.W.B., 1992. Comparison between rough-and smooth-wall turbulent boundary layers. J. Fluid Mech. 245, 599–617.
- Krug, D., Philip, J., Marusic, I., 2017. Revisiting the law of the wake in wall turbulence. J. Fluid Mech. 811, 421–435.
- Kutzbach, J.E., 1961. Investigations of the modification of wind profiles by artificially controlled surface roughness. Studies of the Three-Dimensional Structure of the Planetary Boundary Layer, pp. 71–113.
- Legg, B.J., Long, I.F., Zemroch, P.J., 1981. Aerodynamic properties of field bean and potato crops. Agric. Meteorol. 23, 21–43.
- Leonardi, S., Castro, I.P., 2010. Channel flow over large cube roughness: a direct numerical simulation study. J. Fluid Mech. 651, 519–539.
- Lettau, H., 1969. Note on aerodynamic roughness-parameter estimation on the basis of roughness-element description. J. Appl. Meteorol. 8 (5), 828–832.
- Lien, F.S., Yee, E., 2005. Numerical modelling of the turbulent flow developing within and over a 3-d building array, part iii: a distributed drag force approach, its implementation and application. Boundary-Layer Meteorol. 114 (2), 287–313.
- Macdonald, R.W., Griffiths, R.F., Hall, D.J., 1998a. An improved method for the estimation of surface roughness of obstacle arrays. Atmos. Environ. 32 (11), 1857–1864.
- Macdonald, R.W., Hall, D.J., Walker, S., 1998b. BRE Client Report CR. Wind Tunnel Measurements of Wind Speed within Simulated Urban Arrays, 243/98. Building Research Establishment.
- Macdonald, R.W., 2000. Modelling the mean velocity profile in the urban canopy layer. Boundary-Layer Meteorol. 97 (1), 25–45.
- Mache, M., 2012. Représentation multi-échelle des transferts entre couche de canopée urbaine et atmosphère à l'échelle de la ville (Doctoral dissertation, Ecole centrale de Nantes)
- Manes, C., Poggi, D., Ridolfi, L., 2011. Turbulent boundary layers over permeable walls: scaling and near-wall structure. J. Fluid Mech. 687, 141–170.
- Masters, F., Gurley, K.R., 2003. Non-Gaussian simulation: cumulative distribution function map-based spectral correction. J. Eng. Mech. 129 (12), 1418–1428.

- Mohammad, A.F., Zaki, S.A., Hagishima, A., Ali, M.S.M., 2015. Determination of aerodynamic parameters of urban surfaces: methods and results revisited. Theor. Appl. Climatol. 122 (3–4), 635–649.
- Oke, T.R., Mills, G., Christen, A., Voogt, J.A., 2017. Urban Climates. Cambridge University Press.
- Panofsky, H.A., Dutton, J.A., 1983. Atmospheric Turbulence. General Characteristics of Atmospheric Turbulence (Chapter 5).
- Placidi, M., Ganapathisubramani, B., 2015. Effects of frontal and plan solidities on aerodynamic parameters and the roughness sublayer in turbulent boundary layers. J. Fluid Mech. 782, 541–566.
- Plate, E.J., 1995. Urban climates and urban climate modelling: an introduction. Wind Climate in Cities. Springer Netherlands, pp. 23–39.
- Ramirez, N., Afshari, A., Norford, L., 2018. Validation of simplified urban-canopy aerodynamic parametrizations using a numerical simulation of an actual downtown area. Boundary-Layer Meteorol. 168 (1), 155–187.
- Raupach, M.R., Thom, A.S., Edwards, I., 1980. A wind tunnel study of turbulent flow close to regularly arrayed rough surfaces. Boundary-Layer Meteorol. 18, 373–397.
- Raupach, M.R., 1981. Conditional statistics of Reynolds stress in rough-wall and smooth-wall turbulent boundary layers. J. Fluid Mech. 108, 363–382.
- Raupach, M.R., Coppin, P.A., Legg, B.J., 1986. Experiments on scalar dispersion within a model plant canopy part I: the turbulence structure. Boundary-Layer Meteorol. 35 (1–2), 21–52.
- Raupach, M.R., Antonia, R.A., Rajagopalan, S., 1991. Rough-wall turbulent boundary layers. Appl. Mech. Rev. 44 (1), 1–25.
- Raupach, M., 1992. Drag and drag partition on rough surfaces. Boundary-Layer Meteorol. 60 (4), 375–395.
- Raupach, M.R., Hughes, D.E., Cleugh, H.A., 2006. Momentum absorption in rough-wall boundary layers with sparse roughness elements in random and clustered distributions. Boundary-Layer Meteorol. 120 (2), 201–218.

- Rona, A., Grottadaurea, M., 2010. Generalized Coles' law and outer layer conformal mapping. J. Hydraul. Res. 48 (5), 674–679.
- Schlichting, H., 1979. Boundary Layer Theory. McGraw-Hill Book Co., New York.
- Shao, Y., Yang, Y., 2008. A theory for drag partition over rough surfaces. J. Geophys. Res.: Earth Surface 113 (F2).
- Shaw, R.H., Pereira, A.R., 1982. Aerodynamic roughness of a plant canopy: a numerical experiment. Agric. Meteorol. 26 (1), 51–65.
- Sutton, O.G., 1949. Atmospheric Turbulence. Methuen, London.
- Sutton, O.G., 1953. Micrometeorology. McGraw-Hill. Inc., New York.
- Tani, I., 1987. Turbulent boundary layer development over rough surfaces. Perspectives in Turbulence Studies. Springer, Berlin, Heidelberg, pp. 223–249.
- Theurer, W., Baechlin, W., Plate, E.J., 1992. Model study of the development of boundary layers above urban areas. J. Wind Eng. Ind. Aerod. 41 (1–3), 437–448.
- Thole, K.A., Bogard, D.G., 1996. High Freestream Turbulence Effects on Turbulent Boundary Layers.
- Thom, A.S., 1971. Momentum absorption by vegetation. Q. J. R. Meteorol. Soc. 97 (414), 414–428.
- Tian, G., 2018. Analysis of the Unsteady Boundary-Layer Flow over Urban-like Canopy Using Large Eddy Simulation. Doctoral dissertation).
- Weber, R.O., 1999. Remarks on the definition and estimation of friction velocity. Boundary-Layer Meteorol. 93 (2), 197–209.
- Wooding, R.A., Bradley, E.F., Marshall, J.K., 1973. Drag due to regular arrays of roughness elements of varying geometry. Boundary-Layer Meteorol. 5 (3), 285–308.
- Yang, X.I., Sadique, J., Mittal, R., Meneveau, C., 2016. Exponential roughness layer and analytical model for turbulent boundary layer flow over rectangular-prism roughness elements. J. Fluid Mech. 789, 127–165.